UNIVERSITY OF TARTU

Faculty of Science and Technology

Institute of Chemistry

Anastasiya Ivashyna

Electrode materials for water splitting in alkaline electrolysis

Bachelor's Thesis (12 ECTS)

Curriculum Science & Technology

Supervisor:

PhD Vitali Grozovski

Tartu 2026

Electrode materials for water splitting in alkaline electrolysis

Abstract

Alkaline water electrolysis is a leading pathway to renewable hydrogen production, yet conventional immersed-electrode systems are constrained by bubble-induced mass transport losses and sluggish reaction kinetics. This study investigates NiMo cathodes and NiFe anodes fabricated by galvanostatic electrodeposition onto stainless steel mesh substrates (#300 and #400) for operation in a capillary-fed electrolysis cell, which supplies electrolyte via capillary action through a porous separator, enabling near bubble-free operation. The influence of mesh geometry, fluoropolymer chemistry (PTFE vs. PVDF), coating morphology, gas removal efficiency, and full-cell performance was evaluated in 1 M KOH. SEM and EDS confirmed Volmer–Weber island growth on both substrates, with the #400 mesh supporting higher nucleation density and more uniform elemental distribution. Three-electrode measurements showed NiMo reduces η10 by 222 mV and NiFe reduces η100 by 72–79 mV relative to uncoated #400 substrates. In full-cell testing, the #400 PTFE configuration achieved 1.85 V at 0.5 A and 2.18 V at 1.5 A, compared to 2.49 V at 1.5 A for the polymer-free baseline. Post-operation EDS revealed severe Mo leaching in NiMo cathodes and beneficial Fe enrichment in NiFe anodes consistent with active NiFeOOH reconstruction. The results demonstrate that full-cell performance is governed by the interaction between mesh pore geometry and fluoropolymer surface energy rather than intrinsic catalyst activity alone, with the #400 mesh paired with PTFE identified as the optimal configuration within the tested parameter space.

Keywords: alkaline water electrolysis, Ni-Mo cathode, Ni-Fe anode, electrodeposition, stainless steel mesh, hydrogen evolution.

CERCS: T150, P401

Elektroodimaterjalid vee lagundamiseks aluselisel elektrolüüsil

Lühikokkuvõte

Leeliselise vee elektrolüüs on üks juhtivaid viise taastuva vesiniku tootmiseks, kuid tavapäraseid sukeldatud elektroodidega süsteeme piiravad mullide põhjustatud massiülekandekaod ja aeglane reaktsioonikineetika. Käesolevas uuringus uuriti NiMo katoode ja NiFe anoode, mis valmistati galvanostaatilise elektrosadestamise teel roostevabast terasest võrgust aluspindadele (#300 ja #400) kasutamiseks kapillaartoitmisega elektrolüüsirakus. Selline rakk varustab elektrolüüti kapillaarjõudude toimel läbi poorse separaatori, võimaldades peaaegu mullivaba töörežiimi. Võrgu geomeetria, fluoropolümeeri keemia (PTFE vs. PVDF), katte morfoloogia, gaaside eemaldamise tõhususe ja täisraku jõudluse mõju hinnati 1 M KOH lahuses. SEM ja EDS kinnitasid Volmeri-Weberi saarkasvu mõlemal aluspinnal, kusjuures #400 võrk soodustas suuremat nukleatsioonitihedust ja ühtlasemat elementjaotust. Kolmeelektroodilised mõõtmised näitasid, et NiMo vähendas η10 väärtust 222 mV võrra ja NiFe vähendas η100 väärtust 72–79 mV võrra võrreldes katmata #400 aluspindadega. Täisraku katsetes saavutas #400 PTFE konfiguratsioon 1,85 V voolutugevusel 0,5 A ja 2,18 V voolutugevusel 1,5 A, võrreldes polümeerivaba baasvariandi 2,49 V-ga voolutugevusel 1,5 A. Tööjärgne EDS näitas NiMo katoodides ulatuslikku Mo leostumist ning NiFe anoodides soodsat Fe rikastumist, mis on kooskõlas aktiivse NiFeOOH rekonstrueerumisega. Tulemused näitavad, et täisraku jõudlust määrab üksnes katalüsaatori sisemise aktiivsuse asemel pigem võrgusilma pooride geomeetria ja fluoropolümeeri pinnaenergia vastastikmõju. Testitud parameetrite vahemikus osutus optimaalseks konfiguratsiooniks #400 võrk koos PTFE-ga.

Võtmesõnad: leeliselise vee elektrolüüs, Ni-Mo katood, Ni-Fe anood, elektrosadestamine, roostevaba terasest võrk, vesiniku eraldumine.

CERCS: T150, P401

TABLE OF CONTENTS

ABBREVIATIONS

AEM – Anion Exchange Membrane

AWE – Alkaline Water Electrolysis

CFE – Capillary-fed Electrolysis

CV – Cyclic Voltammetry

EDS – Energy Dispersive X-ray Spectroscopy

HER – Hydrogen Evolution Reaction

OER – Oxygen Evolution Reaction

PEM – Polymer Electrolyte Membrane (or Proton Exchange Membrane)

SEM – Scanning Electron Microscopy

wt% – Weight percentage

INTRODUCTION

Global energy demand continues to grow, driven by population growth, expanding urban infrastructure, and industrial development. Although renewable technologies are being deployed at an increasing pace, fossil fuels remain the dominant source of global energy, supplying close to 80% of total primary energy consumption [1], and their combustion remains the largest contributor to anthropogenic greenhouse gas emissions [2]. Achieving international climate targets therefore requires both a rapid reduction in fossil fuel use and large-scale expansion of renewable power generation, as outlined in the IEA Net Zero Emissions pathway for 2050 [3]. However, renewable sources are inherently intermittent — electricity generation depends on weather conditions, seasonal variability, and geographic location, creating challenges for grid stability, energy storage, and long-distance energy transport [4].

Hydrogen offers a promising solution as an energy carrier capable of storing excess renewable electricity and delivering it on demand. When produced using renewable electricity, green hydrogen provides a near-zero carbon fuel with high gravimetric energy density, applicable across transportation, chemical manufacturing, and power generation, either directly as a fuel or reconverted to electricity via fuel cells [5]. Despite this potential, approximately 95% of global hydrogen is currently generated through carbon-intensive processes such as steam methane reforming and coal gasification [6].

Water electrolysis represents one of the most direct pathways for sustainable hydrogen generation. Driven by electrical energy, the process splits water into hydrogen and oxygen at two electrodes: the hydrogen evolution reaction (HER) at the cathode and the oxygen evolution reaction (OER) at the anode. In alkaline systems specifically, performance is constrained by sluggish reaction kinetics at both electrodes and by mass transport losses associated with gas bubble accumulation at the electrode surface, making catalyst design and electrode architecture central to improving overall efficiency [7]. In this context, transition-metal alloys such as nickel–iron (NiFe) and nickel–molybdenum (NiMo) have demonstrated competitive OER and HER activity respectively as cost-effective alternatives to platinum-group catalysts [8, 9].

This thesis investigates how mesh substrate geometry and fluoropolymer chemistry jointly govern the electrochemical performance of electrodeposited NiFe and NiMo catalysts in a capillary-fed alkaline electrolysis cell. Catalytic coatings were fabricated via controlled

galvanostatic electrodeposition on stainless steel meshes of two grades (#300 and #400), allowing systematic variation of alloy composition and surface morphology. Electrochemical performance toward HER and OER was assessed through cyclic voltammetry and full-cell polarisation measurements, while scanning electron microscopy (SEM) and energy-dispersive X-ray spectroscopy (EDS) were employed to characterise coating morphology, elemental distribution, and post-operation structural evolution. By correlating electrochemical performance with material structure, this work demonstrates that full-cell performance in capillary-fed electrolysis is governed not by intrinsic catalyst activity alone, but by the interaction between mesh pore geometry and polymer wettability — with the #400 mesh paired with PTFE identified as the optimal electrode configuration within the tested parameter space.

1 LITERATURE REVIEW

1.1 Water Electrolysis Technologies

Water electrolysis is a well-established method based on the electrochemical splitting of water using electrical energy to produce hydrogen and oxygen. When powered by renewable electricity, electrolysis enables the generation of green hydrogen and oxygen without direct carbon emissions. Several technologies have been developed, differing mainly in electrolyte type, membrane design, operating conditions and catalyst characteristics [10].

Alkaline water electrolysis (AWE) is the most mature and commercially established technology for large-scale hydrogen production. The electrolyte is a concentrated aqueous alkaline solution (25–40 wt%), typically potassium hydroxide (KOH) or sodium hydroxide (NaOH) and two electrodes are separated by a diaphragm or porous membrane that prevents gas mixing while allowing ionic transport. Non-noble metal catalysts, such as nickel-based materials, keep capital costs low (900–1700 €/kW), and installations have demonstrated lifetimes exceeding 15 years at megawatt scale [10]. Its main limitations are relatively low current density (<0.45 A/cm²) and slower dynamic response to fluctuating power input, yet these have not prevented widespread industrial deployment [10].

Proton exchange membrane electrolysis (PEM) employs a solid polymer membrane that conducts protons from the anode to the cathode, enabling compact cell design and operation at high current densities of up to several A cm^{-2}. However, a strong acidic environment requires noble metal catalysts such as platinum and iridium, which increases material costs and limits widespread large-scale implementation [11].

Anion exchange membrane electrolysis (AEM) has emerged as a hybrid approach combining features of both AWE and PEM systems. An anion-conducting membrane is used to transport hydroxide ions, while allowing the use of non-noble metal catalysts, retaining the advantages of a solid electrolyte - compact design, reduced gas crossover, and operation with distilled water or dilute alkaline solutions. Current limitations centre on membrane degradation under concentrated alkaline conditions and insufficient hydroxide conductivity at elevated current densities, which restrict long-term operational stability [12].

1.2 Capillary-Fed Electrolysis

Conventional alkaline water electrolyzers operate with electrodes fully immersed in a liquid electrolyte. As gas bubbles form and accumulate on electrode surfaces during evolution reactions, active catalytic sites become partially blocked, inducing mass-transport limitations through counter-current gas-liquid flows and increasing ohmic losses in the bulk electrolyte layer between the electrodes. Subsequent cell designs have reduced these losses incrementally, as illustrated in Figure 1.

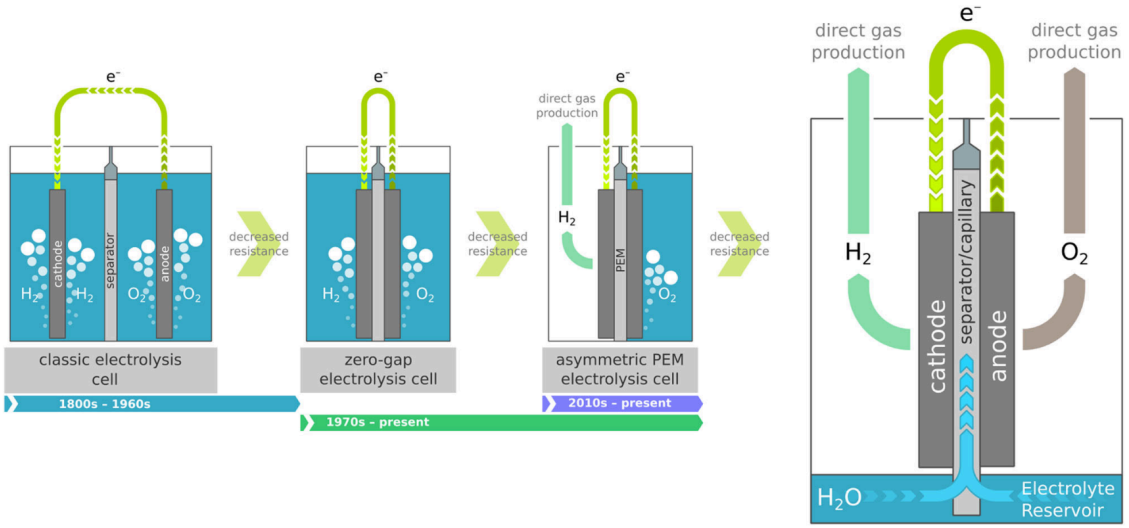

Figure 1. Evolution of water electrolysis cell architectures from conventional immersed alkaline cells to zero-gap, asymmetric PEM, and capillary-fed electrolysis (CFE) configuration. Reproduced from [13].

Zero-gap configurations reduce the inter-electrode distance by pressing the electrodes against a porous separator, shortening the ionic transport pathway and lowering ohmic resistance. However, gas bubbles still form at the electrode surfaces and must migrate through the liquid electrolyte, retaining two-phase transport losses.

Asymmetric proton exchange membrane electrolysers replace the liquid electrolyte gap with a thin solid polymer membrane, generating one product gas directly into a collection chamber and eliminating bubble formation on that side. Nevertheless, bubbles continue to evolve at the opposite electrode, and the technology still requires noble-metal catalysts together with ultra-pure water.

The capillary-fed electrolysis (CFE) concept overcomes these constraints by supplying electrolyte exclusively through capillary-induced transport along a porous inter-electrode

separator rather than by bulk immersion [13]. The lower edge of a hydrophilic porous separator, typically polyethersulfone (PES) with an average pore diameter of 8 μm, is immersed in electrolyte, and spontaneous capillary action draws it upward through the separator. This in-plane flow reaches the electrodes pressed against opposite faces of the separator above the liquid level, maintaining a thin electrolyte film over the catalytic surfaces while evolved gases migrate into adjacent collection chambers. As a result, the system enables near bubble-free operation: gas nucleation at the electrode surface is largely suppressed, keeping the majority of active catalytic sites accessible, and counter-current multiphase flows are eliminated [13].

The separator's high porosity (≈80 %) and relatively large pore size yield low ionic resistance while still sustaining the electrolyte flux required for current densities up to 1 A cm^{-2} at 80–85 °C [13]. Additional wettability control is achieved by incorporating hydrophobic polytetrafluoroethylene (PTFE) within the anode catalyst layer, which promotes bubble detachment and facilitates gas removal from the electrode–electrolyte interface, reducing blockage of active sites during operation. The referenced work also identifies elongated PTFE features that may contribute to gas release, though the primary performance gain is attributed to increased surface hydrophobicity rather than morphology [13].

The CFE architecture reduces cell resistance by more than 270 mΩ cm^2 compared to conventional zero-gap cells employing the same catalysts and electrolyte [13]. Experimentally, a CFE cell with a NiFeOOH anode and Pt/C cathode delivered a voltage of 1.51 V at 0.5 A cm^{-2} and 85 °C, corresponding to 98 % energy efficiency on the higher-heating-value basis and an energy consumption of 40.4 kWh kg^{-1} H_2 — surpassing both commercial alkaline and PEM electrolysers. Faradaic efficiency approached 100 %, with hydrogen crossover remaining below 0.14 vol % even at high current densities [13].

Beyond electrochemical performance, eliminating bulk gas–liquid two-phase flow reduces system complexity by removing the need for electrolyte circulation pumps, gas–liquid separator and cooling systems, resulting in a markedly simpler balance of plant.

1.2.1 Advantages and Limitations of the Capillary-Fed Approach

The CFE configuration combines selected advantages of conventional alkaline, zero-gap alkaline, and PEM electrolysers while mitigating drawbacks. Conventional alkaline electrolysers suffer from high ohmic resistance, extensive bubble coverage of active sites, and

pronounced mass-transport limitations at elevated current densities. Zero-gap designs reduce electrode spacing to lower ionic resistance yet retain concentrated electrolyte and diaphragms, thereby permitting gas crossover and continued bubble accumulation. PEM systems eliminate the liquid electrolyte gap entirely, achieving high ionic conductivity, effective gas separation, and compact cell geometry, but require expensive noble-metal catalysts and corrosion-resistant hardware [11].

In contrast, the CFE employs a porous separator that supplies electrolyte via capillary action, forming thin electrolyte films directly at the electrode surfaces, substantially reducing ohmic resistance, minimising bubble adhesion, accelerating gas detachment, while retaining non-precious-metal catalysts and alkaline operating conditions [13].

Stable CFE operation demands precise control of separator wettability, pore-size distribution, and electrolyte delivery. Deviations can cause electrode flooding or local dry-out, either of which disrupts the thin-film electrolyte supply and degrades performance. The porous transport layer and associated hydrophobic coatings increases fabrication complexity and raises concerns regarding long-term mechanical integrity and chemical stability under concentrated alkaline conditions [13].

1.3 Nickel–Molybdenum cathode materials

Nickel-molybdenum alloys are well-established non-noble electrocatalysts for the hydrogen evolution reaction (HER) in alkaline media, demonstrating competitive activity at current densities relevant to industrial water electrolysis (>100 mA cm^{-2}) [9]. Their advantage over platinum-group catalysts lies not only in lower cost but in the synergistic interaction between Ni and Mo, which modifies hydrogen binding energetics and promotes water dissociation in ways that pure nickel cannot achieve alone [9].

In alkaline media, HER proceeds through three elementary steps. The Volmer step involves electrochemical water dissociation to generate adsorbed hydrogen (H*) and hydroxide ions:

$$H_2O + e^- \rightarrow H^* + OH^- \qquad (1)$$

H* is then removed either via the Heyrovsky step, involving electrochemical desorption:

$$H^* + H_2O + e^- \rightarrow H_2 + OH^- \qquad (2)$$

or via the Tafel step, involving recombination of two adsorbed hydrogen atoms:

$$2H^* \rightarrow H_2 \quad (3)$$

Unlike acidic HER, alkaline HER is kinetically hindered by the additional energy barrier associated with water dissociation, which requires breaking the O–H bond before hydrogen adsorption can occur. Pure nickel is limited by suboptimal hydrogen adsorption energy and sluggish water dissociation kinetics [9]. Incorporation of molybdenum into the nickel lattice addresses both constraints: Mo sites promote hydrogen adsorption and facilitate spillover between Ni and Mo atoms, while DFT calculations show that optimised Ni-Mo phases such as Ni_4Mo exhibit a hydrogen adsorption free energy (ΔG_{H^*}) closer to thermoneutral and lower water dissociation barriers than pure Ni [9].

Several strategies have been established to enhance NiMo catalytic performance beyond intrinsic alloying effects. Morphology engineering through three-dimensional electrode architectures increases electrochemically active surface area, improves bubble detachment, and reduces mass-transport limitations at elevated current densities - electrodeposited NiMo coatings frequently develop porous or hierarchical structures that support these effects [14]. At the electronic level, alloy composition and phase structure govern the d-band centre of the Ni–Mo system, controlling the hydrogen adsorption-desorption balance, varying the Ni:Mo ratio has been shown to optimise intrinsic site activity independently of morphology [9]. Electrodeposition is particularly well-suited to implementing both strategies simultaneously, as it allows controllable regulation of coating thickness, composition, and surface roughness in a single fabrication step, while also influencing nucleation behaviour and interfacial structure in ways relevant to capillary-fed cell integration [14].

1.4 Nickel–Iron anode materials

Nickel–iron based materials are among the most active non-noble electrocatalysts for the oxygen evolution reaction (OER) in alkaline media. [8]. Their high activity originates from the incorporation of iron into nickel hydroxide or oxyhydroxide structures, which modifies the electronic structure of nickel and stabilises high-valence Ni^{3+}/Ni^{4+} species under anodic polarisation, the redox states considered responsible for OER activity [8].

In alkaline media, OER proceeds via a four-electron mechanism involving surface-bound intermediates (Me–OH, Me–O, Me–OOH), producing molecular oxygen:

$$4OH^- \rightarrow O_2 + 2H_2O + 4e^- \quad (4)$$

The active phase is not identical to the as-deposited material. During anodic operation, nickel hydroxide is oxidised to NiOOH-like phases, while iron incorporation modifies charge distribution across Ni–O–Fe linkages, generating the catalytically active configuration in situ [8]. This reconstruction is a defining characteristic of NiFe-based anodes and distinguishes their operational behaviour from their as-deposited structure.

Electrodeposition enables simultaneous co-deposition of nickel and iron, producing alloy-like structures or mixed NiFe hydroxide phases on conductive substrates with controllable composition, morphology, and thickness, while maintaining good electrical contact and mechanical stability [15]. The porous morphologies that frequently result from electrodeposition promote rapid oxygen bubble detachment and reduce active site blockage at elevated current densities. Post-deposition incorporation of PTFE increases surface hydrophobicity, further accelerating oxygen release and reducing local resistive losses during high-current OER operation [13].

It should be noted that similar performance enhancements can arise from unintended iron incorporation from electrolyte impurities or cell components, highlighting the sensitivity of nickel-based electrodes to trace iron species [16].

1.5 Electrodeposition of metal catalysts

Electrodeposition is an electrochemical method for fabricating metallic and alloy catalysts directly on conductive substrates. By adjusting electrolyte composition, pH, temperature, applied current or potential, and deposition time, the deposit composition, thickness, and morphology can be precisely controlled. Alloy coatings are formed by co-deposition of multiple metal ions from a single plating bath. Direct deposition onto conductive metallic supports ensures good electrical contact, mechanical stability, and a scalable fabrication route well-suited to alkaline electrolysis applications [15].

1.5.1 Iron incorporation in Ni-based anodes

Trace iron incorporation into nickel-based electrodes has been widely reported to enhance OER performance. Iron species, whether originating from electrolyte impurities or corrosion of stainless-steel cell components, can adsorb and incorporate into the surface of nickel electrodes, forming highly active NiFe oxyhydroxide phases. Experimental studies demonstrate that increasing iron concentration reduces both HER and OER overpotentials by approximately 100–200 mV [17], and ppm-level iron concentrations are sufficient to produce

measurable activity gains [16]. This has motivated the deliberate incorporation of iron into nickel-based electrode formulations, as in the NiFe coatings investigated in the present work, while also highlighting the sensitivity of nickel-based electrodes to trace metal species and the importance of electrolyte purity control in benchmarking studies.

1.5.2 NiFe Anode Electrodeposition

Iron can be intentionally incorporated during electrodeposition by adding Fe^{2+} or Fe^{3+} salts into the plating bath, enabling NiFe alloys to be formed throughout the porous electrode structure. Upon anodic activation in alkaline electrolyte, the deposited alloy transforms into the catalytically active NiFeOOH phase, providing superior OER activity and enhanced stability compared with pure nickel electrodes [17].

1.5.3 NiMo Cathode Electrodeposition

NiMo electrodeposition relies on induced co-deposition, where molybdenum oxoanions are reduced in the presence of nickel ions and complexing agents such as citrate, forming amorphous or nanocrystalline coatings. The composition and morphology of the deposits depend strongly on bath composition, current density, pH, and temperature [18]. Higher current densities and elevated citrate concentrations, for example, have been shown to favour Mo incorporation and finer grain structures, directly influencing HER activity [19].

1.6 Electrochemical Characterisation: Cyclic Voltammetry

Cyclic voltammetry (CV) is the primary technique used to investigate electrode processes and evaluate electrocatalytic activity. The potential applied to the working electrode is varied linearly with time while the resulting current response is recorded, allowing identification of oxidation and reduction processes occurring at the electrode-electrolyte interface.

The applied potential follows a triangular waveform, swept from an initial value to a predetermined switching potential and then reversed back to the starting value (Figure 2). The slope of this potential sweep defines the scan rate (v), typically expressed in V s^{-1}. The resulting current (I) is plotted as a function of potential (E) to produce a cyclic voltammogram (Figure 3) [20].

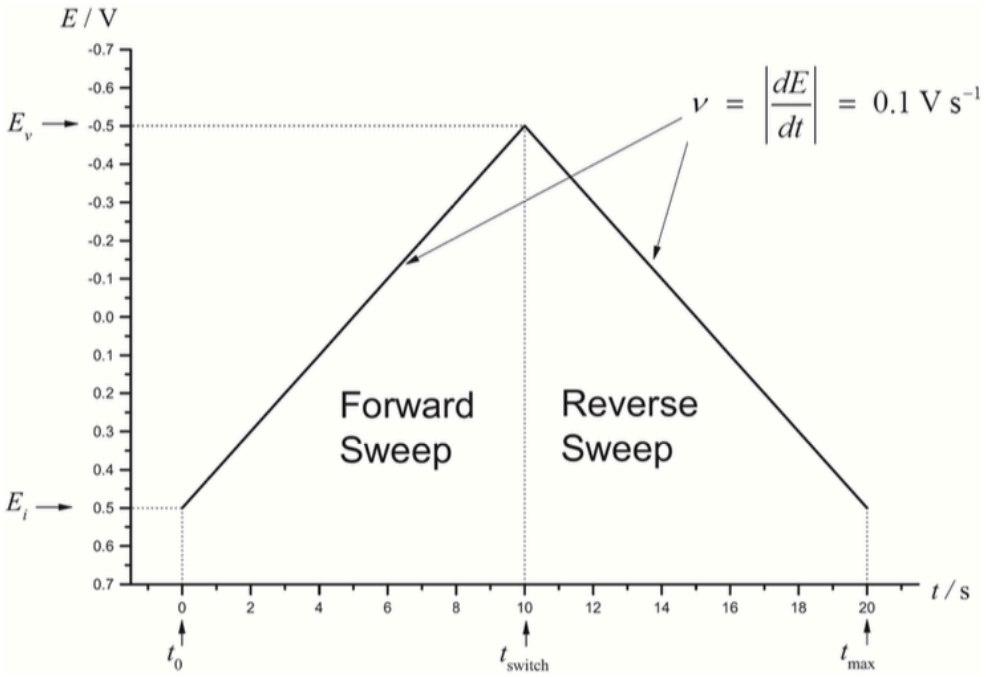

Figure 2. Triangular potential waveform applied during cyclic voltammetry. Reproduced from [20].

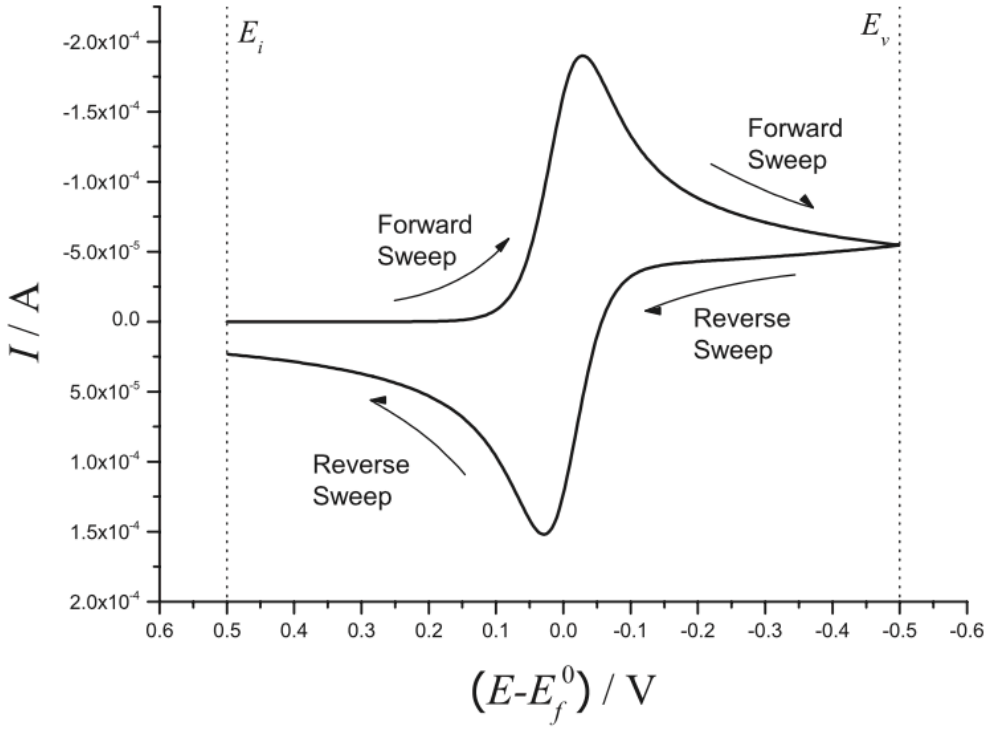

Figure 3. Typical cyclic voltammogram obtained using a triangular potential sweep. Reproduced from [20].

When scanning from more negative to more positive potentials, anodic currents correspond to oxidation processes; the reverse sweep reveals reduction processes. The presence of peaks or

waves in the current–potential curve indicates electrochemical transformations, while their shape and position provide insight into reaction kinetics and surface properties. The shape of the voltammetric response and the comparison between forward and reverse scans can indicate whether the process is reversible, diffusion-controlled, or influenced by surface adsorption [21].

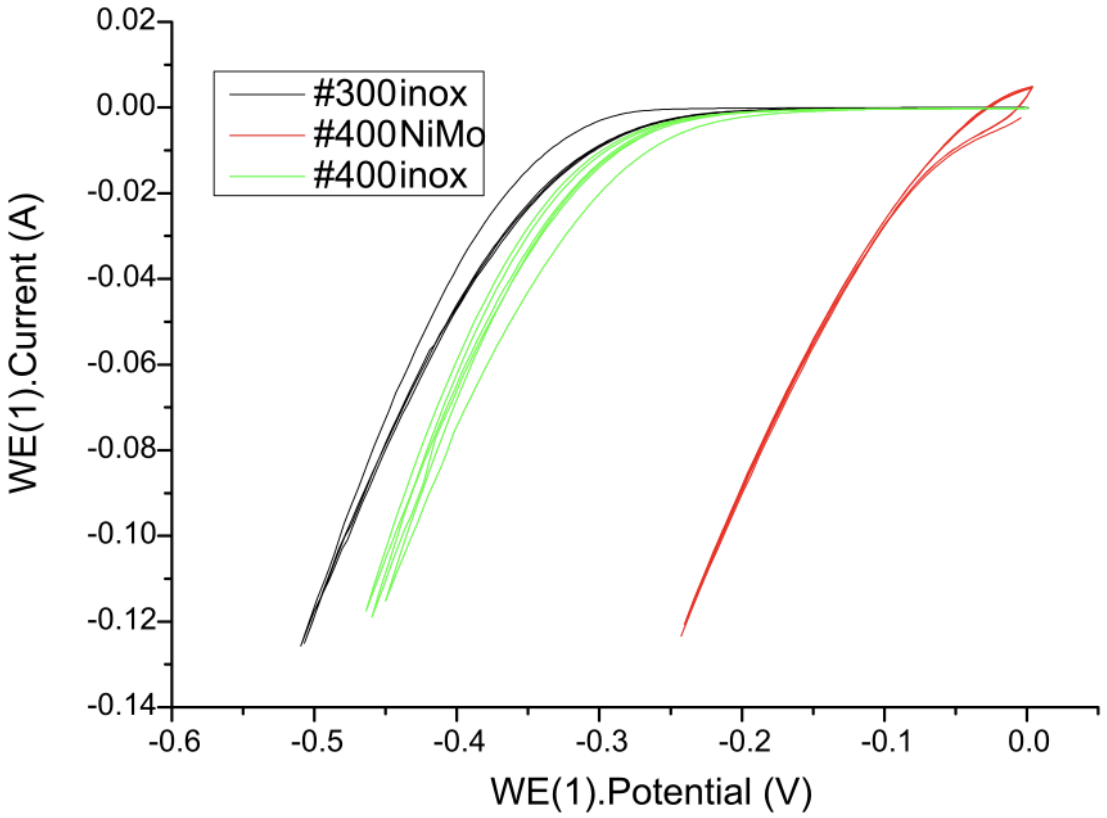

Figure 4. Cyclic voltammograms of stainless steel (inox abbr.) and NiMo-coated electrodes recorded in 1 M KOH aqueous electrolyte at a scan rate $v = 50$ mV·s^{-1}.

Figure 4 illustrates cyclic voltammograms obtained for stainless steel and NiMo-coated mesh electrodes in alkaline electrolyte. In systems dominated by electrocatalytic reactions such as hydrogen evolution, cyclic voltammograms often do not exhibit distinct redox peaks but instead show a monotonic increase in cathodic current with decreasing potential. In such cases, the onset potential of the cathodic current provides information about catalytic activity, while the magnitude and slope of the current response reflect reaction kinetics and charge-transfer efficiency. Hysteresis between forward and reverse scans typically reflects bubble accumulation during gas evolution, with the reverse scan recovering a higher fraction

of accessible active sites. Cyclic voltammetry thus provides a practical basis for comparing electrocatalytic performance even in the absence of well-defined redox peaks.

1.7 Structural and Compositional Characterisation

1.7.1 Scanning Electron Microscopy (SEM)

Scanning electron microscopy (SEM) images surface morphology and microstructure by rastering a focused electron beam across the sample and detecting the resulting signals. Primary electrons penetrate the material and generate signals within an interaction volume whose size depends on accelerating voltage and atomic number, determining both spatial resolution and information depth [22].

Secondary electrons, emitted from within a few nanometres of the surface due to their low energy, provide high-resolution topographic contrast that reveals surface features such as roughness, porosity, cracks, and particle boundaries. Edges and protrusions emit more secondary electrons and appear brighter, while recessed or shadowed regions appear darker [22].

Backscattered electrons originate from deeper within the material and provide complementary compositional contrast: their intensity increases with atomic number, so regions enriched in heavier elements appear brighter. This makes backscattered electron imaging useful for identifying compositional variations, phase distribution, and inhomogeneities within deposited coatings, albeit at lower spatial resolution than secondary electron imaging [22].

1.7.2 Energy-Dispersive X-ray Spectroscopy (EDS)

Energy-dispersive X-ray spectroscopy (EDS), coupled with SEM, enables elemental analysis through the detection of characteristic X-rays emitted when inner-shell electrons are ejected by the primary beam and replaced by higher-energy electrons, producing element-specific emission spectra [23].

EDS allows both qualitative and semi-quantitative determination of elemental composition, as well as spatially resolved elemental mapping, making it well-suited for confirming alloy formation, assessing elemental distribution, and identifying compositional gradients within electrodeposited coatings [23].

2 THE AIMS OF THE THESIS

This thesis investigates the fabrication and characterisation of nickel-based electrode materials for the hydrogen and oxygen evolution reactions in a capillary-fed alkaline electrolysis cell. The work examines how mesh substrate geometry and fluoropolymer chemistry influence catalytic activity and full-cell efficiency:

1. Nickel-based catalysts were fabricated by galvanostatic electrodeposition onto stainless steel mesh substrates of two grades. The resulting electrode morphology and elemental composition were characterised as a function of substrate geometry and deposition conditions. Hydrophobic coatings based on PTFE and PVDF were subsequently applied to investigate their influence on electrolyte distribution, gas bubble detachment, and electrochemical performance in the capillary-fed configuration.
2. The electrodes were characterised using scanning electron microscopy (SEM) and energy-dispersive X-ray spectroscopy (EDS) to examine surface morphology, coating distribution, and elemental composition before and after electrochemical testing. Electrochemical performance was evaluated by cyclic voltammetry (CV) in three-electrode configuration and by full-cell polarisation measurements in two-electrode configuration, enabling comparison of coated and uncoated electrodes across different mesh grades and catalyst compositions.

The results are interpreted in terms of the relationship between electrode structure, surface wettability, and catalytic activity, with the broader goal of identifying electrode configurations suited to efficient capillary-fed alkaline electrolysis.

3 EXPERIMENTAL PART

3.1 MATERIALS AND METHODS

3.1.1 Chemicals and instrumentation

Nickel(II) sulfate hexahydrate ($NiSO_4 \cdot 6H_2O$, Sigma-Aldrich, ACS reagent, ≥98%), iron(III) nitrate nonahydrate ($Fe(NO_3)_3 \cdot 9H_2O$, Sigma-Aldrich, ACS reagent, ≥98%), sodium molybdate dihydrate ($Na_2MoO_4 \cdot 2H_2O$, Sigma-Aldrich, ACS reagent, ≥99%), potassium hydroxide (KOH, Merck, EMSURE® ACS pellets), hydrochloric acid (HCl, Fluka/Honeywell, puriss. p.a., ≥37%), polytetrafluoroethylene (PTFE, 60 wt% dispersion in H_2O, Sigma-Aldrich), poly(vinylidene fluoride) (PVDF, average Mw ≈ 530,000, Sigma-Aldrich), acetone (Sigma-Aldrich, ACS reagent, ≥99.5%), trisodium citrate ($Na_3C_6H_5O_7$, Sigma-Aldrich, ACS reagent, ≥99%), boric acid (H_3BO_3, Sigma-Aldrich, ACS reagent, ≥99%), ammonium chloride (NH_4Cl, Sigma-Aldrich, ACS reagent, ≥99%), and polyethylene glycol (PEG 8000, Sigma-Aldrich, average Mw ≈ 8000) were used as received. Ultrapure water (18.2 MΩ cm, Milli-Q purification system, Millipore) was used for preparation of all solutions.

All chemicals and metal meshes were weighed using an analytical balance (Kern ALJ 200-5DA) before and after electrodeposition.

Electrodeposition of catalyst layers was performed using a Rigol DP932A programmable power supply. Electrochemical measurements were carried out in a conventional three-electrode polypropylene (PP) cell using a Multi Autolab/M204 potentiostat/galvanostat equipped with the FRA32M module (Metrohm, The Netherlands). Data acquisition was controlled using NOVA 2.1 software, and further data processing was performed using OriginPro 8.5.

The working electrode was a catalyst-modified twill-woven stainless steel filter mesh (HTP, China, SS304, mesh numbers - lines per inch: #300 and #400) with an exposed surface area 1.0 cm^2. A nickel mesh (Dongfu, China, Nickel N6, #40) served as the counter electrode, while a reversible hydrogen electrode (RHE) placed in the same electrolyte with an entrapped hydrogen bubble was used as the reference electrode.

Full-cell measurements were performed using a custom-fabricated capillary-fed (Hysata-type) electrolysis cell made from PTFE. The cell separator was a polyethersulfone

(PES) membrane with a nominal pore size of 8 µm (Sterlitech Corporation, USA). Cyclic voltammetry measurements were carried out in Ar-saturated 1 M KOH at scan rates between 10 and 50 mV s^{-1}.

3.1.2 Electrode preparation and catalyst deposition

Catalyst layers were electrodeposited onto stainless steel mesh substrates of grades #300 and #400. Prior to deposition, the meshes were degreased in acetone, rinsed with ultrapure water, and activated in 3 M hydrochloric acid (HCl) to remove surface oxides. After activation, the substrates were thoroughly rinsed with ultrapure water and immediately transferred to the plating bath. The exposed deposition area was defined as 1 cm^2. In all depositions, the stainless steel mesh served as the working electrode and a nickel mesh (#40) as the counter electrode.

NiFe electrodeposition

The NiFe plating solution consisted of 0.2 M $NiSO_4$, 1.5 M NH_4Cl, 0.012 M $Fe(NO_3)_3$, and 0.114 M HCl. Polyethylene glycol (PEG 8000, 0.2 g L^{-1}) was added as a structure-directing additive. Electrodeposition was performed galvanostatically in two steps: a nucleation step at 10 mA cm^{-2} for 300 s, followed by a growth step at 2 A cm^{-2} for 40 s. The obtained electrodes are denoted as NiFe-300 and NiFe-400.

NiMo electrodeposition

The NiMo plating bath contained 0.1 M $NiSO_4$ and 0.01 M Na_2MoO_4 as metal ion sources., with trisodium citrate (0.25 M) added as a complexing agent to stabilise molybdate species and prevent precipitation, and boric acid (0.05 M) as a buffering agent. Electrodeposition was carried out galvanostatically at 1 A cm^{-2} for 10 min. The resulting electrodes are denoted #300 NiMo and #400 NiMo.

3.1.3 Faradaic efficiency determination

The Faradaic efficiency (FE) of the electrodeposition process was evaluated by comparing the experimentally measured mass of deposited material with the theoretical mass calculated using Faraday's law of electrolysis.

The theoretical mass of deposited metal was calculated as:

$$m_{theoretical} = \frac{QM}{nF} \quad (5)$$

where Q is the total charge passed (C), M is the molar mass of nickel (58.69 g mol^{-1}), n is the number of electrons for Ni^{2+} reduction, and F is Faraday's constant (96485 C mol^{-1}).

Nickel was taken as the primary electroactive species in both systems, acknowledging that co-deposited Fe or Mo contributes additional mass not captured by this estimate. The number of electrons involved in the reduction was taken from the reaction:

$$Ni^{2+} + 2e^{-} \rightarrow Ni \quad (6)$$

Accordingly, the value $n = 2$ was used in all calculations.

The total charge was determined from:

$$Q = It \quad (7)$$

where I is the applied current (A) and t is the deposition time (s).

The experimental mass (m_{actual}) was determined by weighing the stainless steel mesh substrates before and after electrodeposition using an analytical balance. Faradaic efficiency was then calculated as:

$$FE = \frac{m_{actual}}{m_{theoretical}} \times 100\% \quad (8)$$

The standard deviation of the Faradaic efficiency values was calculated according to:

$$\sigma = \sqrt{\frac{1}{N-1}\sum_{i=1}^{n}(x_i - \bar{x})^2} \quad (9)$$

where x_i represents individual Faradaic efficiency values, $\bar{x}$ is the average value, and N is the number of measurements.

Faradaic Efficiency of NiFe

The total charge passed during the process was calculated from the applied current and deposition time for both stages of the process (10 mA cm^{-2} for 300 s and 2 A cm^{-2} for 40 s), yielding a total charge of 83 C.

Using Eq. (5), the theoretical deposited mass was calculated as:

$$m_{theoretical} = \frac{83 \times 58.69}{2 \times 96485} = 0.025245\ g$$

The experimentally measured mass differences for six independently prepared electrodes ranged from 0.01049 g to 0.01179 g (Annex A1.1). The corresponding Faradaic efficiencies varied between 41.57% and 46.71%, and a mean of 45.16%, with a standard deviation of 1.95%, calculated according to Eq. (9).

Faradaic Efficiency of NiMo

For NiMo deposition, a constant current density of 1 A cm^{-2} was applied for 10 min. For an electrode area of 1 cm^2, this corresponds to a total deposition time of 600 s, resulting in a total charge of 600 C.

The theoretical mass was calculated using the same assumption of nickel as the dominant electroactive species. Using Eq. (5), the theoretical deposited mass was calculated as:

$$m_{theoretical} = \frac{600 \times 58.69}{2 \times 96485} = 0.182494\ g$$

The experimentally measured mass differences ranged from 0.00193 g to 0.00252 g (Annex A1.2). The corresponding Faradaic efficiencies were between 1.06% and 1.38%, and a mean of 1.19 ± 0.12%.

The average Faradaic efficiency for NiMo deposition was 1.19%, with a standard deviation of 0.12%, calculated according to Eq. (9). The low Faradaic efficiency of 1.19% indicates that the majority of applied charge was consumed by competing HER. This is attributed to the low Ni^{2+} concentration (0.1 M) and strong citrate complexation of both Ni and Mo ions, which reduce metal ion availability at the electrode surface and shift the cathodic process predominantly toward proton/water reduction rather than metal deposition [24].

3.1.4 Polymer coating (PVDF and PTFE)

After electrodeposition, selected samples were coated with fluoropolymers to improve surface wettability and catalyst adhesion. Both polymers were applied by dipping the electrode into the respective solution and drying on a hotplate at 65 ^{o}C, five dipping–drying cycles were performed for each sample to ensure uniform coverage.

PVDF solution (~1 wt%) was prepared by dissolving poly(vinylidene fluoride) in boiling acetone with continuous stirring under reflux until complete dissolution, then cooled to room temperature before use. For PTFE coating, a 60 wt% PTFE aqueous dispersion was used as received and diluted with ultrapure water prior to application to 1.25%.

3.1.5 Physical characterisation

The morphological structure of the synthesized materials was investigated using scanning electron microscopy (SEM) and energy dispersive X-ray spectroscopy (EDS). SEM was performed using a Zeiss EVO MA15 microscope operating in variable pressure mode at a chamber pressure of 30 Pa. Imaging was carried out at an accelerating voltage of 25 kV and a probe current of 30 μA using a backscattered electron (BSE) detector. EDS analysis was conducted using an Oxford X-Max energy-dispersive detector with an active area of 80 mm². SEM samples were prepared by cutting small pieces of the catalyst-coated mesh and fixing them onto carbon adhesive tape mounted on an SEM sample holder. The samples were introduced into the microscope without further treatment.

4 RESULTS AND DISCUSSION

This section evaluates the physicochemical and electrochemical properties of Ni-based electrocatalysts deposited on stainless steel mesh substrates (#300 and #400) via electrodeposition. The investigation focuses on how mesh structure and hydrophobic polymer chemistry influence the morphological evolution, elemental distribution, and subsequent electrocatalytic activity toward the HER and OER in 1 M KOH,

Physical characterisation through SEM and EDS was employed to elucidate the nucleation mechanisms and coating integrity, subsequently correlated with electrochemical performance metrics derived from Cyclic Voltammetry (CV).

4.1 Morphological Analysis of As-Deposited Catalysts

Figure 5 presents SEM images of the bare stainless steel mesh substrates (#300 and #400) prior to catalyst deposition, highlighting their geometric and surface characteristics.
At low magnification (Fig. 5 A, B), both meshes exhibit the typical twill-woven architecture of commercial stainless steel filter meshes, with defined wire intersections and uniform periodicity. A clear distinction between the two substrates is observed: the #400 mesh displays a significantly higher wire density and smaller pore openings compared to the #300 mesh. Based on scale bar measurements from SEM micrographs, the #300 mesh shows apertures of ~40–60 μm, while the #400 mesh shows ~20–30 μm. This reduction in size is expected to yield a higher geometric surface area per unit volume, consistent with the finer wire packing of the #400 grade.

At higher magnification (Fig. 5 C, D), the individual wires appear relatively smooth with only minor longitudinal striations likely from the manufacturing process. The absence of significant surface defects or microstructuring suggests a limited density of intrinsic nucleation sites. This baseline state suggests that subsequent nucleation will be more strongly influenced by the substrate's interfacial chemistry and local current distribution than by mechanical anchoring at surface defects.

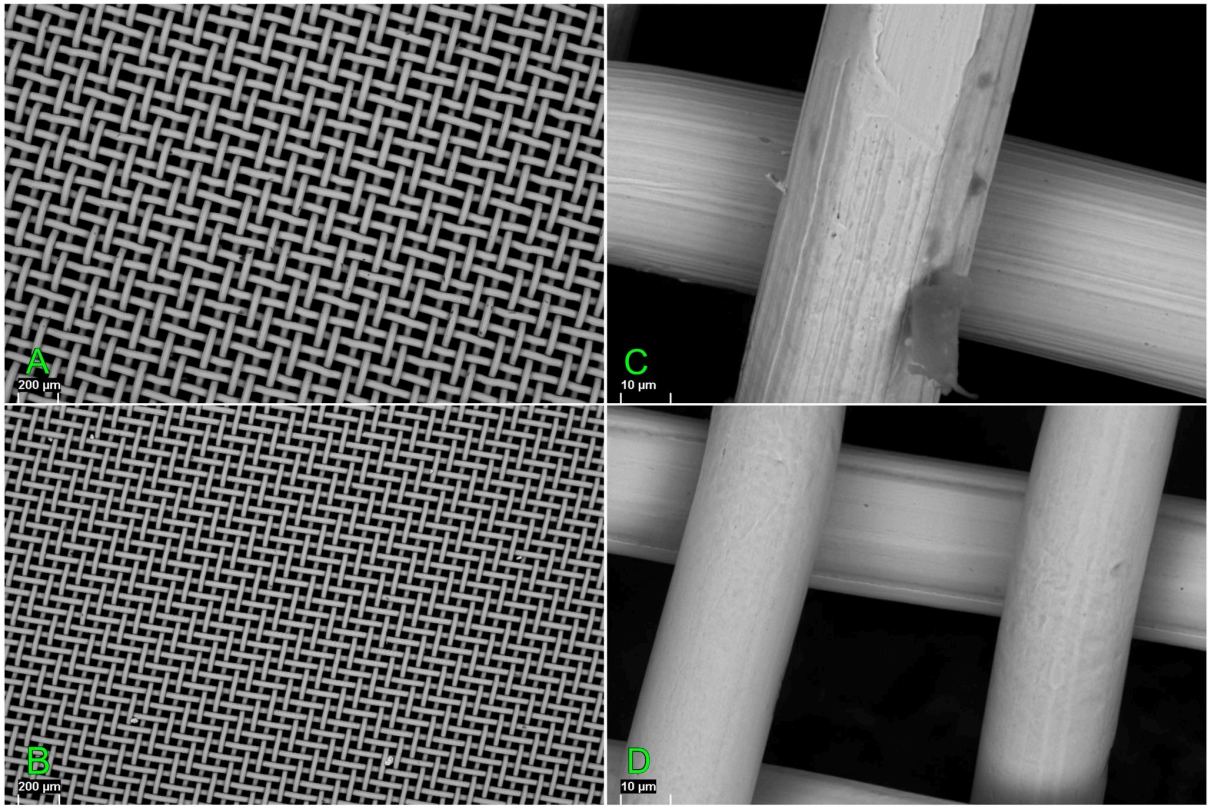

Figure 5. SEM images of bare stainless steel meshes (#300 and #400) before electrodeposition. (A, B) Low magnification showing mesh geometry and density. (C, D) Higher magnification showing wire surface morphology.

Figure 6 illustrates the surface morphology of the electrodeposited catalysts prior to electrochemical testing. At low magnification (Fig. 6 A–D), a non-uniform distribution is evident across all samples, with deposition occurring as discrete islands and clusters rather than a continuous film, indicative of a nucleation-limited "island growth" (Volmer-Weber) mechanism, where the initial metal nuclei form at localised active sites rather than spreading into a uniform layer. This behaviour is likely driven by the Cr-rich passive oxide layer (~2–5 nm) inherent to 304 stainless steel, which is not completely removed by HCl activation and persists as an electrically resistive barrier to uniform metal nucleation [25, 26].

The #300 mesh (Fig. 6A, B) shows a patchy distribution with low apparent nucleation density and large regions of exposed wire. In contrast, the #400 mesh (Fig. 6C, D) supports a significantly higher density of deposition sites, resulting in a more integrated coating appearance. The finer wire diameter and reduced aperture size of the #400 mesh promote a more uniform local current density during the initial plating stage.

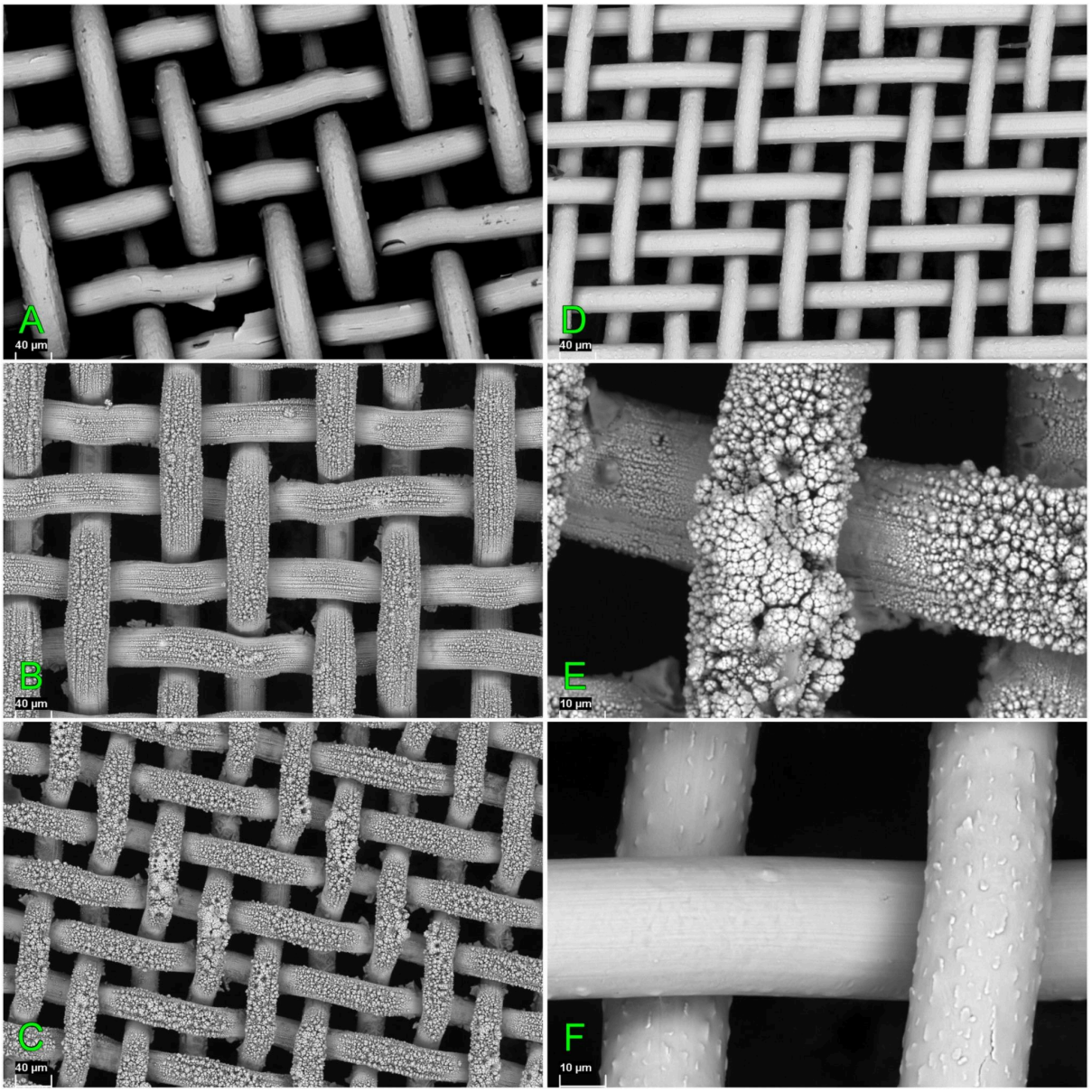

Figure 6. SEM images of NiFe and NiMo coatings electrodeposited on stainless steel meshes (#300 and #400) before cyclic voltammetry. (A) #300 NiMo, (B) #300 NiFe, (C) #400 NiFe, and (D) #400 NiMo at low magnification, showing the overall coating morphology. Higher-magnification images of (E) #400 NiFe and (F) #400 NiMo, highlighting differences in deposit morphology.

High-magnification imaging of the NiFe coating (Fig. 6 E) reveals a dense, cauliflower-like nodular structure consistent with granular NiFe morphologies reported for similar citrate-free chloride baths [15], which typically correlate with increased electrochemically active surface area.

In contrast, the NiMo coatings (Fig. 6 F) exhibit coarser, compact agglomerates with a layered or "leaf-like" appearance. These clusters appear less uniform in surface coverage compared to the NiFe samples and are consistent with reported observations of NiMo alloys

deposited from complex electrolytes, which often exhibit intergrown spheroidal structures and relatively coarse grain morphology [27]. The coarser clustering in NiMo compared to NiFe may be attributed to induced co-deposition kinetics, where it is proposed that the presence of Mo ions and citrate complexing agents slows the nucleation rate relative to the growth rate, leading to the development of larger primary particles.

Figure 7. EDS elemental maps of NiFe and NiMo coatings electrodeposited on stainless steel meshes (#300 and #400) before cyclic voltammetry. (A) #300 NiMo, (B) #300 NiFe, (C) #400 NiFe, and (D) #400 NiMo, showing the spatial distribution of Ni and Fe across the mesh surface.

EDS elemental maps (Fig. 7 A–D) show that nickel (Ni) is detected across the wire surfaces in all samples, though with heterogeneous intensity that mirrors the island-like deposition morphology. Regions of low Ni signal correspond to areas with a dominant Fe and Cr from

the underlying stainless steel substrate, confirming that substantial fractions of the wire surface remain uncoated or covered only by the native oxide.

Table 1. Semi-quantitative EDS composition (wt%) of NiFe and NiMo coatings electrodeposited on stainless steel meshes (#300 and #400) before cyclic voltammetry.

Sample	Ni (wt%)	Mo (wt%)	Fe (wt%)	Cr (wt%)	O (wt%)
#300 NiMo	37.0 ± 2.3	14.9 ± 2.0	22.8 ± 4.5	6.7 ± 1.2	4.8 ± 1.0
#400 NiMo	44.2 ± 4.5	24.4 ± 5.3	9.1 ± 1.2	2.6 ± 0.3	5.2 ± 0.7
#300 NiFe	80.6 ± 8.2	—	8.6 ± 2.4	1.0 ± 0.5	0.8 ± 0.9
#400 NiFe	84.0 ± 8.1	—	7.8 ± 4.2	0.9 ± 0.9	1.7 ± 1.0

The #400 mesh samples (Fig. 7 C, D) show markedly more homogeneous Ni distribution than #300 mesh (Fig. 7 A, B), consistent with quantitative EDS data (Table 1). For NiMo coatings, Ni content increases from 37.0 ± 2.3 wt% (#300) to 44.2 ± 4.5 wt% (#400), while the substrate Fe signal drops from 22.8 to 9.1 wt% — reflecting the higher nucleation density supported by the finer mesh geometry.

NiFe coatings show substantially higher Ni signal densities (80.6–84.0 wt%) than NiMo across both mesh types, consistent with their denser, more continuous granular structure under equivalent deposition conditions [15]. The comparatively lower and more variable Ni content in NiMo coatings warrants further consideration. Despite using an identical electrolyte composition and stainless steel substrate to those reported in the literature [19], the NiMo coatings in this study exhibit a more heterogeneous elemental distribution. The referenced work achieved uniform Ni and Mo coverage using chronocoulometry at low charge densities, whereas the high-current galvanostatic parameters (1 A cm^{-2}) and substantially higher charge loading (600 C cm^{-2}) employed here appear to promote what may be termed a 'coalescence bottleneck' — a regime in which the system favours progressive growth of discrete Volmer–Weber agglomerates over the formation of a continuous, coalesced film. This highlights that current density and deposition control mode are as critical as bath chemistry in determining the final catalytic surface architecture on mesh supports. The large standard deviations, particularly for #400 NiFe, reflect compositional heterogeneity tied to the spatial distribution of catalyst clusters across the three-dimensional mesh geometry, a consequence of discontinuous coating on an open-mesh substrate.

4.2 Electrochemical characterisation results

The intrinsic electrochemical behaviour of the electrodes was evaluated in 1 M KOH using a standard three-electrode configuration, with all potentials IR-corrected to isolate catalytic activity potential values from ohmic contributions.

Figure 8A shows that the #400 NiMo electrode exhibits the earliest HER onset at approximately −0.025 V vs. RHE, compared to −0.30 V for both bare meshes. At −0.20 V, the #400 NiMo electrode reaches −80 mA cm^{-2}, nearly twice the current density of the uncoated substrates, which remain below −40 mA cm^{-2}.

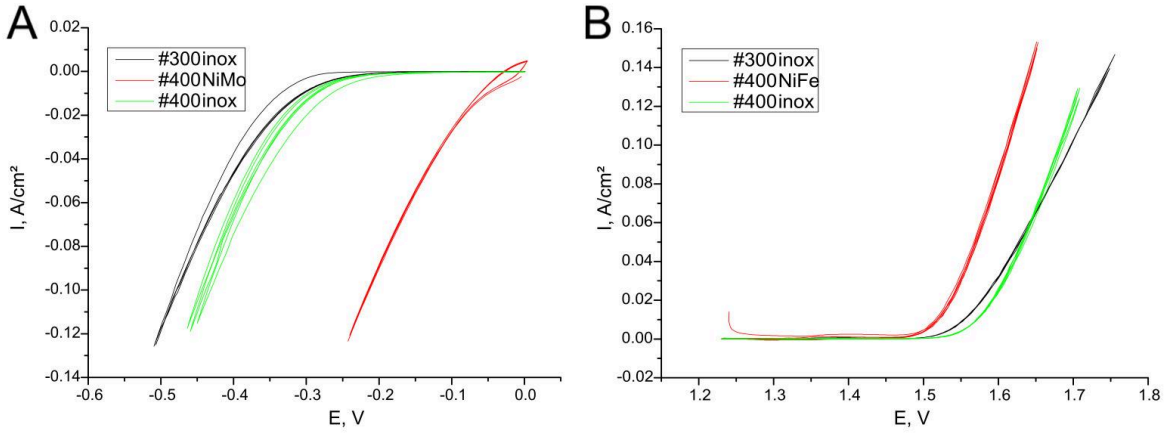

Figure 8. Polarization curves measured in a three-electrode cell in 1 M KOH at room temperature, showing (A) HER activity of #300 inox, #400 inox, and #400 NiMo electrodes, and (B) OER activity of #300 inox, #400 inox, and #400 NiFe electrodes at a scan rate v = 50 mV·s^{-1}.

The bare #300 and #400 inox meshes require overpotentials of 335 mV and 266 mV respectively to reach −10 mA cm^{-2}, with the modest improvement of the #400 mesh likely attributable to its finer wire geometry (Table 2). The #400 NiMo electrode requires only 49 mV at −10 mA cm^{-2} and 211 mV at −100 mA cm^{-2}, a reduction of 222 mV relative to the bare #400 substrate, driven by the synergistic electronic interaction between hyper-d-electronic Ni and hypo-d-electronic Mo, which shifts the hydrogen adsorption free energy (ΔG_{H^*}) closer to the thermoneutral value (≈ 0 eV) [9]. Pure Ni binds hydrogen too strongly ($\Delta G_{H^*} \approx -0.27$ to − 0.30 eV), but alloying-induced modulation of the d-band centre weakens this interaction, bringing ΔG_{H^*} of optimised Ni–Mo phases such as Ni_4Mo to values as low as −0.09 eV, approaching the activity of platinum-group metals on the HER volcano [9].

As these Tafel slopes were extracted from transient cyclic voltammetry scans at 50 mV s^{-1}, they should be treated as apparent values appropriate for relative performance comparison rather than absolute kinetic parameters.

Table 2. Summary of HER electrocatalytic parameters obtained from CV and Tafel analysis for bare and modified stainless steel electrodes in 1 M KOH.

Sample	η10 / mV	η100 / mV	Tafel fitting range / mA cm^{-2}	Tafel slope / mV dec^{-1}	R^2
#300 inox	335	486	10–50	120.2	0.9926
#400 inox	266	433	10–50	139.6	0.9924
#400 NiMo	49	211	10–50	129.3	0.9936

The bare #300 mesh yields a Tafel slope of 120.2 mV dec^{-1}, moderately lower than the 139.6 mV dec^{-1} recorded for the #400 mesh. This is attributed to the coarser geometry of the #300 mesh: its larger apertures (~40–60 μm) reduce local electrolyte confinement and bubble-shielding interference in the 10–50 mA cm^{-2} fitting range, keeping the recorded slope within 0.2 mV dec^{-1} of the theoretical Volmer limit of 120 mV dec^{-1}, effectively matching it. The denser #400 weave, by contrast, may introduce localised ohmic losses within its tighter pore structure, elevating the apparent slope. The NiMo coating partially recovers this, reducing the slope of the #400 substrate from 139.6 to 129.3 mV dec^{-1}, consistent with the Ni–Mo clusters lowering the activation barrier for water dissociation relative to the passive oxide surface of the bare stainless steel.

A lower Tafel slope does not indicate a superior electrode in absolute terms. Despite its lower slope, the bare #300 mesh requires 335 mV to reach −10 mA cm^{-2}, versus only 49 mV for #400 NiMo — a difference of 286 mV. The slope reflects the mechanistic pathway: the overpotential reflects the actual energy cost of driving the reaction at a practically relevant current density. That the #400 NiMo slope sits above that of the bare #300 mesh is an expected outcome given that the NiMo surface is no longer a geometrically uniform wire but a multi-phase cluster morphology, where local adsorption energetics and partial coverage effects, discussed below, alter the apparent slope independently of the substrate geometry.

The value of 129.3 mV dec^{-1} for #400 NiMo is consistent with the 120–140 mV dec^{-1} range typically reported for NiMo alloys in alkaline media, confirming that the Volmer step remains the rate-determining step [18]. The marginal positive deviation from the ideal 120 mV dec^{-1} (at 25 °C) does not indicate a change in mechanism, but rather reflects non-ideal adsorption conditions on the heterogeneous catalyst surface. Specifically, the kinetics likely follow Temkin-type behaviour, where ΔG_{H^*} varies with surface coverage rather than remaining constant as assumed in the ideal Langmuir case [9, 20]. This coverage-dependence is directly linked to the island morphology of the NiMo clusters identified in Section 4.1,where the discontinuous cluster geometry generates site-specific energy variations and partial coverage effects. Additionally, polarisation to higher overpotentials can promote surface hydride formation and subsurface hydrogen absorption in NiMo alloys, introducing a secondary kinetic barrier to charge transfer [18, 19]. Consequently, while water dissociation remains the primary bottleneck, its rate is modulated by the coverage-dependent energetic landscape of the multi-phase Ni–Mo–oxide interface [9, 27].

In the anodic region (Figure 8 B), the #400 NiFe electrode exhibits a lower OER onset of ~1.50 V vs. RHE compared to ~1.60 V for both bare meshes, and achieves a current density exceeding 140 mA cm^{-2} at 1.65 V, versus ~100 mA cm^{-2} for the uncoated substrates. The absence of a well-defined limiting current across the investigated window confirms that the system remains kinetically controlled throughout.

The bare #300 and #400 inox meshes show η10 values of 326 mV and 343 mV respectively, with Tafel slopes of 50.0 and 45.4 mV dec^{-1} respectively (Table 3). The #400 NiFe electrode yields the lowest η10 of 291 mV, below both bare meshes, consistent with its earlier onset potential. The kinetic advantage of the NiFe coating is more reliably captured at higher current densities: η100 decreases from 466 mV (#300 inox) and 459 mV (#400 inox) to 387 mV (#400 NiFe), a reduction of 72–79 mV.

The Tafel slope of 52.1 mV dec^{-1} for #400 NiFe is comparable to that of the bare #300 mesh (50.0 mV dec^{-1}) and marginally higher than #400 inox (45.4 mV dec^{-1}). Given that these slopes were extracted from transient CV scans and the NiFe system undergoes active surface reconstruction during measurement, the slope differences are within the range attributable to measurement artefacts rather than mechanistic change. The intrinsic activity of the reconstructed NiFeOOH phase is better reflected in the η100 reduction of 72–79 mV relative

to the bare substrates, consistent with Fe incorporation into the NiOOH lattice modulating the electronic environment of Fe^{3+} active centres, shifting the OER descriptor ($\Delta G_{O^*} - \Delta G_{OH^*}$) closer to the volcano peak and balancing the adsorption–desorption energetics of OH*, O*, and OOH* intermediates more effectively than the native stainless steel oxide [8].

Table 3. Summary of OER electrocatalytic parameters obtained from CV and Tafel analysis for bare and modified stainless steel electrodes in 1 M KOH.

Sample	η10 / mV	η100 / mV	Tafel fitting range / mA cm^{-2}	Tafel slope / mV dec^{-1}	R^2
#300 inox	326	466	1-10	50.0	0.9962
#400 inox	343	459	1-10	45.4	0.9973
#400 NiFe	291	387	1-10	52.1	0.9963

Overpotentials were calculated relative to the thermodynamic OER potential according to: $\eta = E_{RHE} - 1.23\,V$

Taken together, NiMo reduces η10 by 222 mV relative to the bare #400 substrate, while NiFe reduces η100 by 72 mV, confirming that both coatings meaningfully enhance HER and OER activity respectively in alkaline conditions. Catalyst coatings were applied exclusively to the #400 substrate, as preliminary testing indicated that the #300 mesh geometry was susceptible to electrode flooding under capillary-fed operating conditions, making direct performance comparison between mesh geometries for coated electrodes beyond the scope of this study.

Following the intrinsic kinetic studies, the electrodes were evaluated in a capillary-fed electrolysis (CFE) cell in 1 M KOH to assess performance under operational conditions.

Both configurations show a comparable onset of ~1.50–1.52 V, but diverge sharply as current demand increases. At 0.5 A, the PTFE-modified cell operates at 1.85 V versus 1.99 V for the polymer-free baseline — a 140 mV reduction. This gap widens to 310 mV at 1.5 A (2.18 V vs. 2.49 V). The improvement is attributed to the hydrophobic, aerophilic character of PTFE, which promotes rapid bubble detachment and coalescence, maintaining an effective three-phase boundary within the porous PES separator and preventing active site masking by accumulated gas [13].

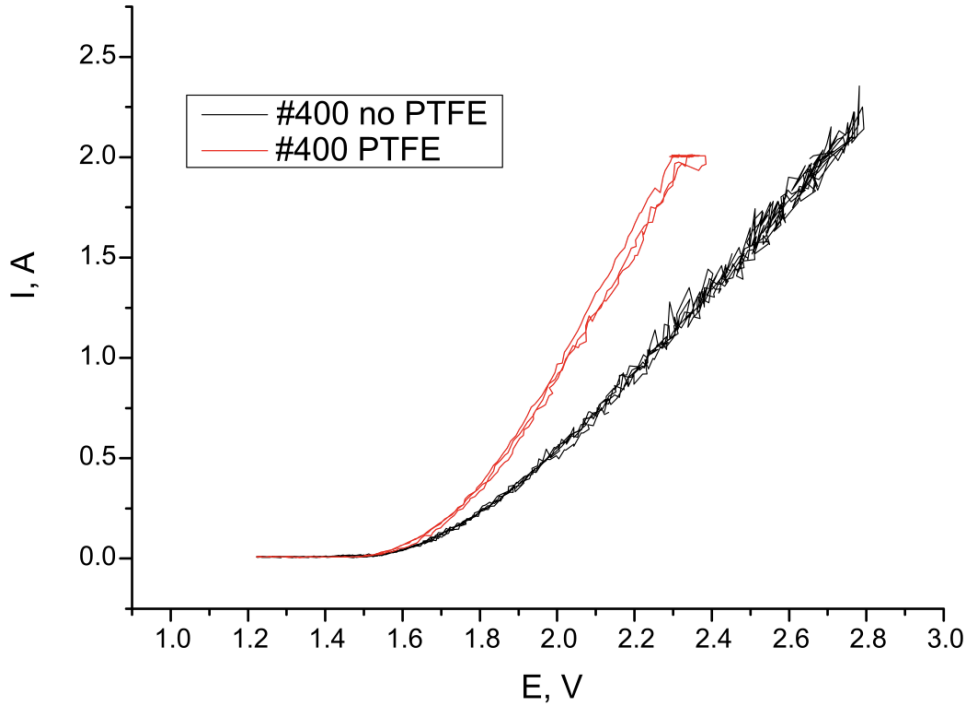

Figure 9. Effect of PTFE on full-cell polarization behavior in 1 M KOH, at a scan rate $v = 50$ mV·s^{-1}.

The PTFE-modified electrode data extends to ~2.0 A, corresponding to the upper current limit of the measurement range, beyond which no data was collected. The polymer-free configuration was measured up to ~2.3 A at 2.8 V, reflecting a wider voltage window applied in that case.

Table 4. Full-cell polarization benchmarks comparing #400 electrodes with and without PTFE in 1 M KOH.

Sample	**E onset (V)**	**V cell 0.5 A (V)**	**V cell 1.0 A (V)**	**V cell 1.5 A (V)**	**V cell 2.0 A (V)**
#400 PTFE	1.50	1.85	2.02	2.18	2.29
#400 no PTFE	1.52	1.99	2.23	2.49	2.68

Values were extracted from the reverse polarization scan, representing the wetted and stabilized electrode state after initial bubble removal and surface activation.

The polymer-free curve also exhibits substantially higher noise at elevated currents, reflecting erratic nucleation and release of large gas bubbles that intermittently block current flow. The smoother PTFE response confirms more stable, continuous gas transport, consistent with reduced ohmic fluctuations reported in optimised capillary-fed architectures [13].

Polymer effectiveness is not determined by its chemistry alone — it is governed by its interaction with the substrate's pore architecture, as the following results demonstrate.

The #400 PTFE configuration delivers the steepest current–voltage response, maintaining a sharp rise throughout the measured current range. In contrast, both PVDF-modified electrodes (#300 and #400) exhibit a more linear, quasi-resistive response, suggesting that bubble retention increases local void fraction within the catalyst layer and elevates effective ohmic resistance even at moderate currents.

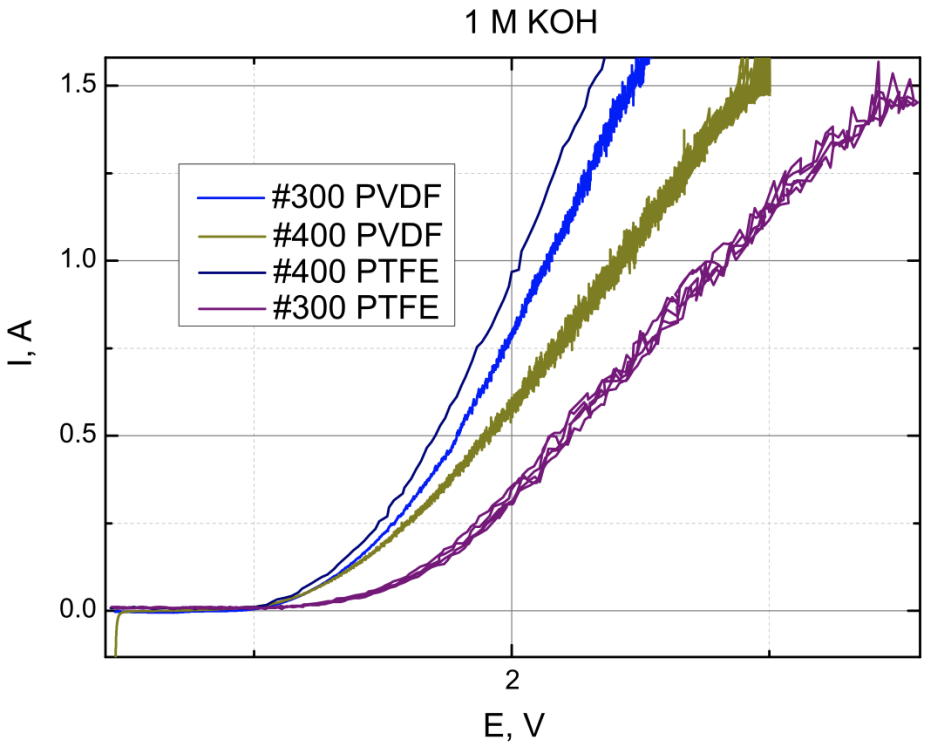

Figure 10. Effect of polymer type (PTFE and PVDF) and mesh grade on full-cell polarization behavior in 1 M KOH at a scan rate $\nu = 50\ mV \cdot s^{-1}$.

Among all configurations, #400 PTFE performs best: 1.85 V at 0.5 A and 2.18 V at 1.5 A. Its advantage over #400 PVDF (1.95 V and 2.50 V at the same currents) is likely reflects the lower surface energy of PTFE (~19 mN m^{-1}) relative to PVDF (~36 mN m^{-1}) [28], which promotes faster bubble coalescence and detachment by forming a discontinuous triple-phase contact line, keeping a higher fraction of active sites wetted during operation [13]. Conversely, the higher surface energy of PVDF results in stronger bubble adhesion and longer residence times, leading to more extensive "gas screening" and higher cell voltages [14].

Table 5. Full-cell polarization benchmarks comparing PTFE- and PVDF-bonded electrodes in 1 M KOH.

Sample	E onset (V)	V cell 0.5 A (V)	V cell 1.0 A (V)	V cell 1.5 A (V)	V cell 2.0 A (V)
#300 PVDF	1.5	1.89	2.07	2.23	2.40
#400 PVDF	1.5	1.95	2.19	2.5	-
#400 PTFE	1.5	1.85	2.02	2.18	2.30
#300 PTFE	1.6	2.14	2.45	2.76	-

Values were extracted from the reverse polarization scan, representing the wetted and stabilized electrode state after initial bubble removal and surface activation.

The poor performance of the #300 PTFE configuration (2.14 V at 0.5 A) suggests a fundamental mismatch between substrate geometry and polymer chemistry. On the coarser #300 mesh (aperture ~40–60 μm), the highly hydrophobic PTFE likely repels electrolyte from the larger pore interiors, preventing adequate wetting of the electrode surface. This causes electrode flooding in the gas-evolution sense, rather than liquid flooding, where the electrolyte film at the electrode surface breaks down, forcing the system into a bubble-nucleation-dominated regime. As gas bubbles accumulate and mask the catalytic surface, the effective electrochemical surface area drops sharply and cell voltage rises steeply, outweighing any benefit from improved gas detachment [29].

In contrast, #300 PVDF (1.89 V at 0.5 A) performs considerably better on the same substrate, consistent with PVDF's higher surface energy allowing partial pore wetting while still providing adequate mechanical support for the catalyst layer.

The data suggests that #400 mesh provides a more stable platform for the PTFE. The smaller apertures (~20–30 μm) of the #400 mesh likely support a more uniform distribution of the hydrophobic polymer, creating more numerous and shorter gas-transport channels. The result is a simultaneous benefit from the higher geometric surface area of the #400 mesh and more efficient gas detachment, mirroring reported results that bubble departure modes are governed by the relationship between pore size and surface wettability [9].

4.3 Post-Electrochemical Characterisation: Structural and Compositional Evolution

Figure 11 presents SEM micrographs of the NiFe and NiMo electrodes following cyclic voltammetry and full-cell polarisation testing. At low magnification (Fig. 11A–D), micro-cracks and partial delamination are visible within the catalyst islands across all samples, concentrated at wire intersections and edges where local current density peaks. This morphological evolution is consistent with mechanical stress imposed by rapid H_2 and O_2 bubble nucleation and detachment, which progressively erodes the Volmer–Weber clusters identified in Section 4.1 [9].

The #400 mesh configurations (Fig. 11C, D) retain a visibly higher fraction of their original catalyst loading than the #300 configurations (Fig. 11A, B). The finer wire geometry of the #400 mesh likely provides a more continuous support network that reduces the mechanical leverage exerted by departing bubbles. The sparser catalyst islands on the #300 mesh wires show more pronounced flaking, indicating that initial nucleation density directly influences long-term structural retention.

High-magnification imaging of the #300 NiFe coating (Fig. 11E) reveals surface roughening and fracturing of the primary cauliflower-like nodules, consistent with the in situ NiFe → NiFeOOH phase transition discussed in Section 4.2. Anodic polarisation and Fe incorporation drive surface-level lattice expansion, increasing active site density while simultaneously generating micro-cracks at the metallic alloy–oxyhydroxide interface due to lattice mismatch [8].

The #400 NiMo configuration (Fig. 11F) presents a distinct degradation profile: deep transcrystalline cracks and visibly thinned agglomerates, consistent with selective Mo leaching in alkaline media, where Mo dissolves as soluble molybdate ions [9]. The resulting Ni-rich framework is mechanically fragile and electronically disrupted, providing a structural basis for the increased cell voltages at high current densities in Section 4.2.

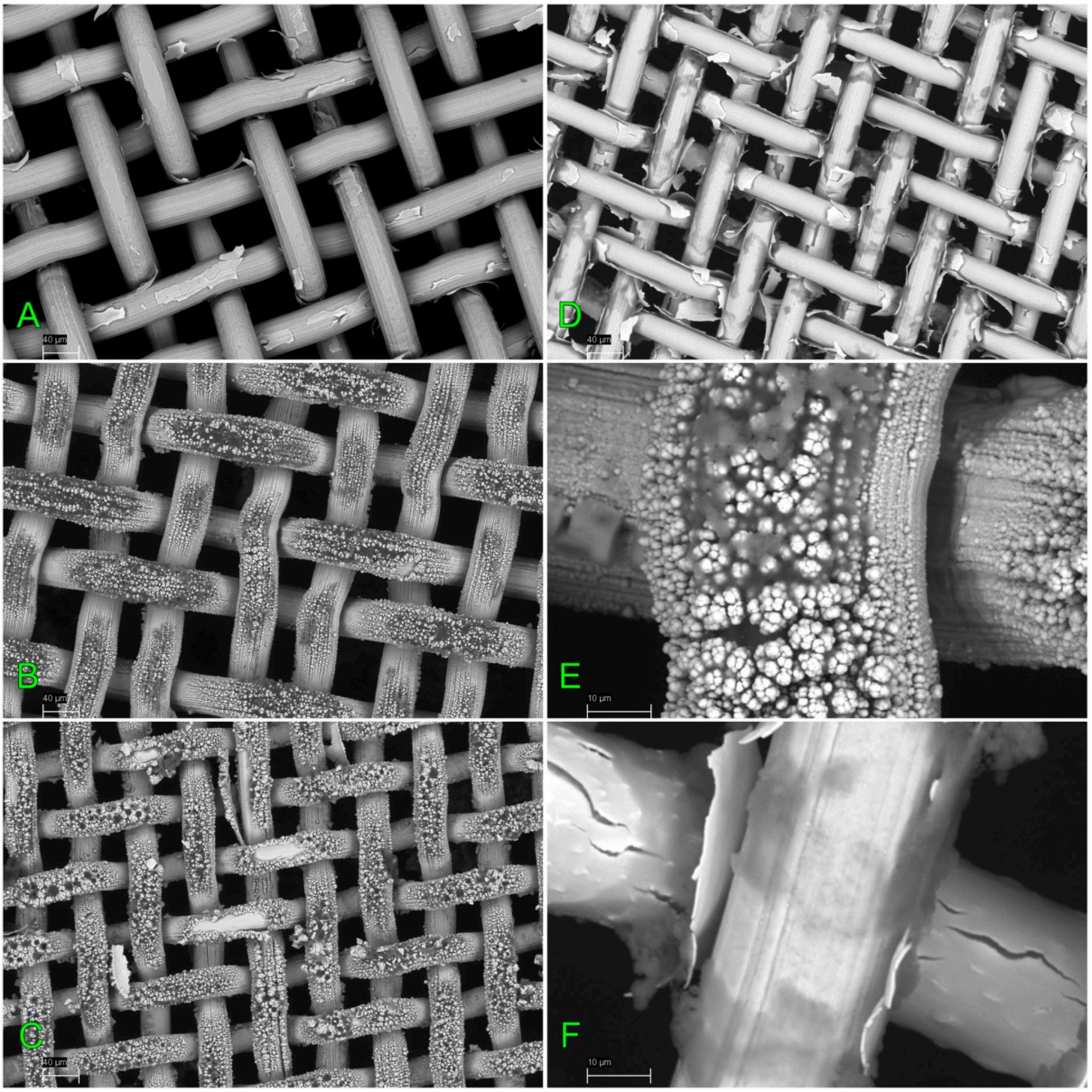

Figure 11. SEM images of NiFe and NiMo coatings on stainless steel meshes (#300 and #400) after cyclic voltammetry. (A) #300 NiMo, (B) #300 NiFe, (C) #400 NiFe, and (D) #400 NiMo at low magnification, showing coating degradation. Higher-magnification images of (E) #300 NiFe and (F) #400 NiMo.

Figure 12 presents EDS elemental maps of all four electrodes after electrochemical operation. The increased visibility of substrate Fe and Cr signals across all samples, relative to the as-deposited state (Fig. 7), confirms that crack propagation and delamination have exposed substantial portions of the underlying stainless steel mesh.

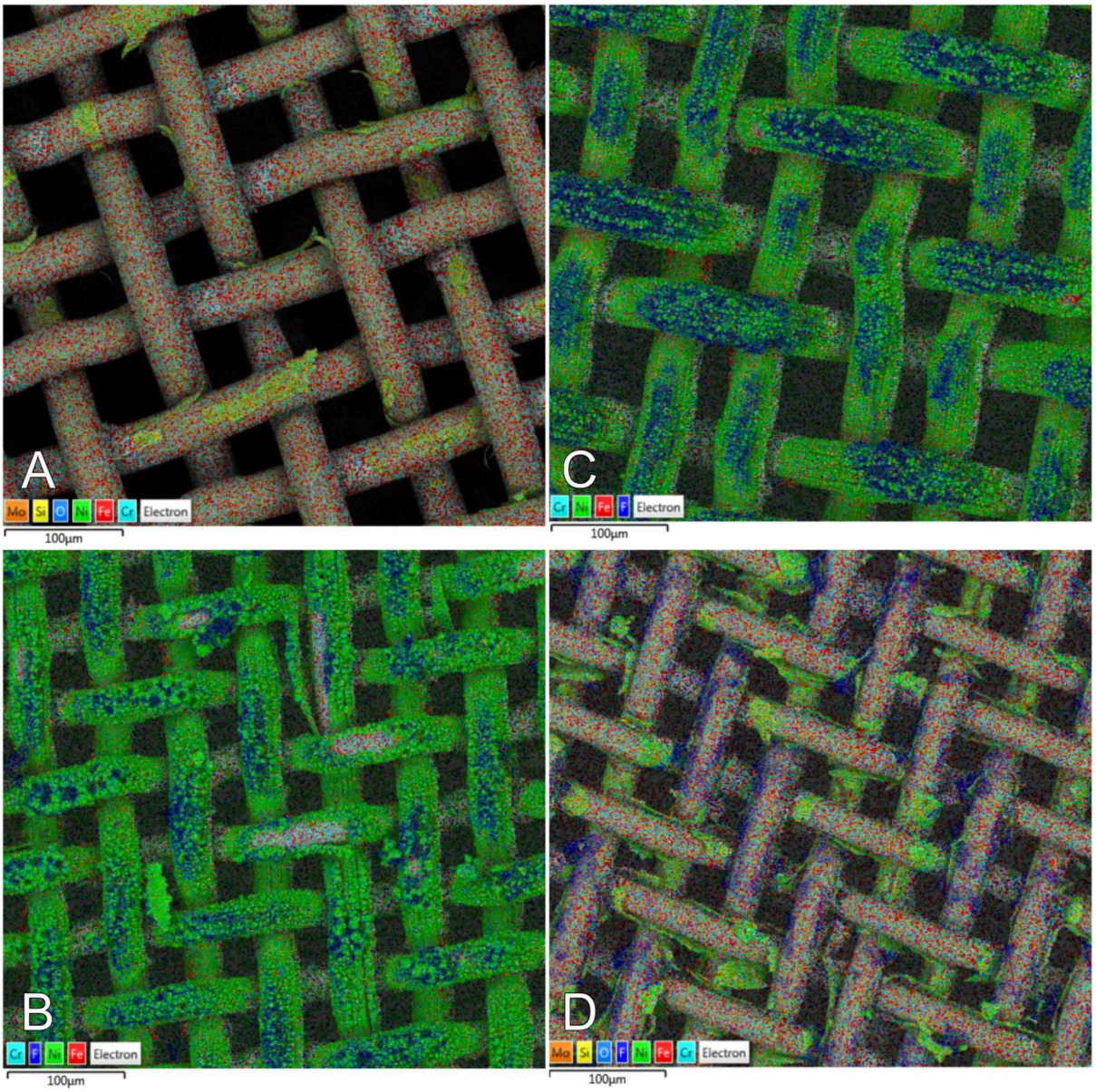

Figure 12. EDS elemental maps of NiFe and NiMo coatings on stainless steel meshes (#300 and #400) after cyclic voltammetry. (A) #300 NiMo, (B) #300 NiFe, (C) #400 NiFe, and (D) #400 NiMo, showing the elemental distribution maps of Ni and Fe and other elements across the mesh surface.

The quantitative data in Table 6 reveals severe Mo depletion in the NiMo cathodes: Mo content in the #400 NiMo electrode dropped from 24.4 ± 5.3 wt% to 4.4 ± 3.7 wt% after operation, with Ni simultaneously falling from 44.2 to 21.5 wt%. The EDS maps (Fig. 12A, D) show a fragmented, discontinuous Ni signal, confirming that the remaining catalyst exists as isolated remnants, consistent with the progressive loss of catalytically active surface area contributing to elevated cell voltages at high current densities..

The NiFe anodes (Fig. 12B, C) show a more stable elemental profile, retaining 66.6 – 68.4 wt% Ni. The #400 NiFe electrode exhibits a near two-fold increase in detected Fe content,

from 7.8 ± 4.2 wt% to 16.3 ± 21.9 wt%. While partial substrate exposure contributes to this, the localised Fe enrichment on Ni-rich regions is consistent with active Fe incorporation from the electrolyte or substrate corrosion products, reconstructing the surface into Fe-rich NiFeOOH — a process documented in the literature as beneficial to OER activity [17, 25]. The denser catalytic coverage retained by the NiFe anodes is consistent with the sustained OER activity reflected in the η100 reduction of 72–79 mV relative to the bare substrates reported in Section 4.2.

Table 6. Semi-quantitative EDS composition (wt%) of NiFe and NiMo coatings electrodeposited on stainless steel meshes (#300 and #400) after cyclic voltammetry.

Sample	Ni (wt%)	Mo (wt%)	Fe (wt%)	Cr (wt%)	O (wt%)	F (wt%)
#300 NiMo	17.3 ± 12.6	3.8 ± 4.9	59.4 ± 14.3	15.6 ± 3.4	2.6 ± 0.9	—
#400 NiMo	21.5 ± 13.0	4.4 ± 3.7	47.5 ± 16.2	13.3 ± 4.0	1.6 ± 1.2	10.8 ± 6.2
#300 NiFe	66.6 ± 10.0	—	7.3 ± 2.5	0.9 ± 0.5	—	25.2 ± 13.2
#400 NiFe	68.4 ± 26.6	—	16.3 ± 21.9	3.7 ± 6.4	0.5 ± 0.7	10.7 ± 7.2

A fluorine signal is detected post-CV across most PTFE/PVDF-coated samples: 10.8 wt% for #400 NiMo, 10.7 wt% for #400 NiFe, and 25.2 wt% for #300 NiFe — where none was present in the as-deposited state, confirming that fluoropolymer residues persist within the catalyst layer after operation. The large standard deviations in F content (e.g., ±13.2 wt% for #300 NiFe) reflect the non-uniform polymer distribution across the three-dimensional mesh geometry. In the #300 configuration specifically, the breakdown of the thin electrolyte film and transition into a bubble-nucleation-dominated regime, discussed in Section 4.2, likely accelerated mechanical detachment of both catalyst material and fluoropolymer from the wire surfaces, contributing to the heterogeneous distribution observed here.

Collectively, the post-CV characterisation reveals mechanistically distinct degradation pathways: NiMo cathodes are primarily limited by chemical instability through Mo leaching, while NiFe anodes undergo partial surface reconstruction through Fe incorporation that partially compensates for mechanical material loss, suggesting that NiFe anodes are better

positioned to maintain catalytic activity under prolonged operation than the Mo-depleted NiMo cathodes, though dedicated stability testing would be required to confirm this.

4.4 Future works

While this study identifies an optimised electrode configuration for mesh-based capillary-fed electrolysis, several directions for further investigation emerge from the results.

Electrodeposition protocol refinement**:** the Faradaic efficiency of 1.19% for NiMo galvanostatic deposition indicates that the overwhelming majority of applied charge was consumed by competing HER, contributing to the coalescence bottleneck and heterogeneous cluster morphology identified in Section 4.1. Future work should investigate pulse electrodeposition or chronocoulometry at lower current densities as alternatives, which may improve nucleation density on the resistive stainless steel oxide layer, increase catalyst yield, and produce more continuous and reproducible coatings.

NiMo cathode stability: post-CV EDS revealed severe Mo depletion, from 24.4 to 4.4 wt% in the #400 NiMo electrode, indicating significant chemical instability under alkaline operating conditions. Future studies should explore protective strategies including chromium barrier coatings [30], carbon encapsulation to inhibit active site dissolution [31], or ternary alloying (e.g., Ni–Mo–W or Ni–Mo–P) to produce more resilient lattice structures that retain Mo species during prolonged cathodic polarisation.

Long-term durability Assessment: the present evaluation was limited to cyclic voltammetry and short-term polarisation scans. Assessment of industrial readiness requires extended chronopotentiometric testing, ideally exceeding 1000 hours, to evaluate mechanical integrity of the Volmer–Weber catalyst clusters under continuous gas evolution stress and to quantify the impact of accumulated impurities, such as dissolved Fe from system corrosion, on full-cell efficiency [13].

SUMMARY

This study evaluated NiMo cathodes and NiFe anodes electrodeposited onto stainless steel mesh substrates (#300 and #400) for capillary-fed alkaline electrolysis, examining how mesh geometry and fluoropolymer chemistry influence coating morphology and full-cell performance in 1 M KOH.

SEM and EDS characterisation confirmed Volmer–Weber island growth on both substrates, with the #400 mesh supporting higher nucleation density and more uniform elemental distribution. The galvanostatic NiMo deposition exhibited a Faradaic efficiency of only 1.19%, attributed to strong citrate complexation and low free metal ion concentration favouring competing HER over metal deposition. Three-electrode CV measurements in 1 M KOH showed NiMo reduces $\eta 10$ by 222 mV and NiFe reduces $\eta 100$ by 72–79 mV relative to uncoated substrates. In full-cell testing, the #400 PTFE configuration achieved 1.85 V at 0.5 A and 2.18 V at 1.5 A, significantly lower than the polymer-free baseline (2.49 V at 1.5 A), driven by the low surface energy of PTFE promoting rapid bubble detachment. The #300 PTFE configuration performed worst, consistent with electrolyte film breakdown and transition into a bubble-nucleation-dominated regime on the coarser mesh. Post-operation analysis revealed severe Mo leaching in NiMo cathodes (from 24.4 to 4.4 wt%), while NiFe anodes showed beneficial Fe enrichment consistent with active NiFeOOH reconstruction.

The results demonstrate that full-cell performance is governed by the interaction between mesh pore geometry and fluoropolymer surface energy, with refined NiMo deposition protocols and improved cathode stability identified as the primary targets for future development.

REFERENCES

[1] International Energy Agency. (2025). *World energy statistics and energy data explorer*. Paris, France: IEA. https://www.iea.org/data-and-statistics

[2] International Energy Agency. (2025). *Energy and CO_2 emissions data explorer*. Paris, France: IEA. https://www.iea.org/data-and-statistics

[3] International Energy Agency. (2023). *Net zero by 2050: A roadmap for the global energy sector* (2023 update). https://www.iea.org/reports/net-zero-by-2050

[4] Lund, P. D., Lindgren, J., Mikkola, J., & Salpakari, J. (2015). Review of energy system flexibility measures to enable high levels of variable renewable electricity. *Renewable and Sustainable Energy Reviews, 45*, 785–807. https://doi.org/10.1016/j.rser.2015.01.057

[5] Dincer, I., & Acar, C. (2015). Review and evaluation of hydrogen production methods for better sustainability. *International Journal of Hydrogen Energy, 40*(34), 11094–11111. https://doi.org/10.1016/j.ijhydene.2014.12.035

[6] Riera, J. A., Lima, R. M., & Knio, O. M. (2023). *A review of hydrogen production and supply chain modeling and optimization*. International Journal of Hydrogen Energy, 48(37), 13731–13755. https://doi.org/10.1016/j.ijhydene.2022.12.242

[7] Carmo, M., Fritz, D. L., Mergel, J., & Stolten, D. (2013). A comprehensive review on PEM water electrolysis. *International Journal of Hydrogen Energy, 38*(12), 4901–4934. https://doi.org/10.1016/j.ijhydene.2013.01.151

[8] Mohammed-Ibrahim, J., & Sun, X. (2020). *A review on NiFe-based electrocatalysts for efficient alkaline oxygen evolution reaction*. Journal of Power Sources, 448, 227375. https://doi.org/10.1016/j.jpowsour.2019.227375

[9] Park, S. H., To, D. T., & Myung, N. V. (2023). A review of nickel-molybdenum based hydrogen evolution electrocatalysts from theory to experiment. *Applied Catalysis A: General, 651*, 119013. https://doi.org/10.1016/j.apcata.2022.119013

[10] Sebbahi, S., Assila, A., Alaoui Belghiti, A., Laasri, S., Kaya, S., Hlil, E. K., Rachidi, S., & Hajjaji, A. (2024). A comprehensive review of recent advances in alkaline water electrolysis for hydrogen production. *International Journal of Hydrogen Energy, 82*, 583–599. https://doi.org/10.1016/j.ijhydene.2024.07.428

[11] Wang, J., Yang, J., Feng, Y., Hua, J., Chen, Z., Liao, M., Zhang, J., & Qin, J. (2025). Comparative experimental study of alkaline and proton exchange membrane water electrolysis for green hydrogen production. *Applied Energy, 379*, 124936. https://doi.org/10.1016/j.apenergy.2024.124936

[12] Li, C., & Baek, J.-B. (2021). The promise of hydrogen production from alkaline anion exchange membrane electrolyzer. *Nano Energy, 87*, 106162. https://doi.org/10.1016/j.nanoen.2021.106162

[13] Hodges, A., Hoang, A. L., Tsekouras, G., Wagner, K., Lee, C.-Y., Swiegers, G. F., & Wallace, G.

G. (2022). A high-performance capillary-fed electrolysis cell promises more cost-competitive renewable hydrogen. *Nature Communications, 13*, 1304. https://doi.org/10.1038/s41467-022-28953-x

[14] Liu, H., Liu, D., Cheng, X., Hua, Z., & He, S. (2022). One-step electrodeposition of Ni–Mo electrode with column–pyramid hierarchical structure for highly efficient hydrogen evolution. *Materials & Design, 224*, 111427. https://doi.org/10.1016/j.matdes.2022.111427

[15] Sakita, A. M. P., Vallés, E., Della Noce, R., & Benedetti, A. V. (2018). Novel NiFe/NiFe-LDH composites as competitive catalysts for clean energy purposes. *Applied Surface Science, 447*, 107–116.https://doi.org/10.1016/j.apsusc.2018.03.235

[16] Rajeev, M., Jerome-Saboori, A., Shekhar, R., Boettcher, S. W., & Kempler, P. A. (2025). Impacts of dissolved iron on alkaline water electrolysis cells. *ACS Catalysis, 15*(5), 2847–2856. https://doi.org/10.1021/acscatal.4c07439

[17] Demnitz, M., Martins Lamas, Y., Garcia Barros, R. L., de Leeuw den Bouter, A., van der Schaaf, J., & de Groot, M. T. (2024). Effect of iron addition to the electrolyte on alkaline water electrolysis performance. *iScience, 27*(1), 108695. https://doi.org/10.1016/j.isci.2023.108695

[18] Manazoğlu, M., Hapçı, G., & Orhan, G. (2016). Electrochemical deposition and characterization of Ni-Mo alloys as cathode for alkaline water electrolysis. *Journal of Materials Engineering and Performance, 25*(1), 130–137. https://doi.org/10.1007/s11665-015-1849-7

[19] Zhiani, M., Taghiabadi, M. M., & Bagherabadi, M. H. (2023). Optimization of Ni-Mo-coated stainless steel as a high-performance cathode in alkaline water electrolysis. *Electrocatalysis, 14*, 473–483. https://doi.org/10.1007/s12678-023-00810-5

[20] Compton, R. G., & Laborda, E. (2020). *Understanding voltammetry: Simulation of electrode processes*. Imperial College Press.

[21] Elgrishi, N., Rountree, K. J., McCarthy, B. D., Rountree, E. S., Eisenhart, T. T., & Dempsey, J. L. (2018). A practical beginner's guide to cyclic voltammetry. *Journal of Chemical Education, 95*(2), 197–206. https://doi.org/10.1021/acs.jchemed.7b00361

[22] Zhou, W., Apkarian, R., Wang, Z. L., & Joy, D. (2006). Fundamentals of scanning electron microscopy (SEM). In W. Zhou & Z. L. Wang (Eds.), *Scanning microscopy for nanotechnology* (pp. 1–40). Springer. https://doi.org/10.1007/978-0-387-39620-0_1

[23] "SEM (Scanning Electron Microscopy) & EDX Analysis Laboratory Services," Lucideon. Accessed: Apr. 30, 2025. [Online]. Available: https://www.lucideon.com/testing-characterisation/techniques/sem-edx

[24] Almeida, A. F. de, Venceslau de Souto, J. I., dos Santos, M. L., Costa de Santana, R. A., Alves, J. J. N., Campos, A. R. N., & Prasad, S. (2021). *Establishing relationships between bath composition and the properties of amorphous Ni–Mo alloys obtained by electrodeposition*. *Journal of Alloys and Compounds*, 888, 161595. https://doi.org/10.1016/j.jallcom.2021.161595

[25] Zamanizadeh, H. R., Sunde, S., Pollet, B. G., & Seland, F. (2022). Tailoring the oxide surface

composition of stainless steel for improved OER performance in alkaline water electrolysis. *Electrochimica Acta, 424*, 140561. https://doi.org/10.1016/j.electacta.2022.140561

[26] Maurice, V., Yang, W. P., & Marcus, P. (1998). X-ray photoelectron spectroscopy and scanning tunneling microscopy study of passive films formed on (100) Fe-18Cr-13Ni single-crystal surfaces. *Journal of The Electrochemical Society, 145*(3), 909–920.https://doi.org/10.1149/1.1838366

[27] Protsenko, V. S., Bobrova, L. S., Butyrina, T. E., Baskevich, A. S., Korniy, S. A., & Danilov, F. I. (2023). Electrodeposited Ni–Mo coatings as electrocatalytic materials for green hydrogen production. *Heliyon, 9*(4), e15230. https://doi.org/10.1016/j.heliyon.2023.e1523.

[28] Fischer, T., Tenbusch, J., Möller, M., & Singh, S. (2022). *A facile method for grafting functional hydrogel films on PTFE, PVDF, and TPX polymers*. *Soft Matter*, 18, 4315–4324. https://doi.org/10.1039/D2SM00313A

[29] Zappia, M. I., Bellani, S., Zuo, Y., Ferri, M., Drago, F., Manna, L., & Bonaccorso, F. (2022). *High-current density alkaline electrolyzers: The role of Nafion binder content in the catalyst coatings and techno-economic analysis*. Frontiers in Chemistry, 10, 1045212. https://doi.org/10.3389/fchem.2022.1045212

[30] Peng, L., Min, J., Bendavid, A., Chu, D., Lu, X., Amal, R., & Han, Z. (2022). *Stabilizing the unstable: Chromium coating on NiMo electrode for enhanced stability in intermittent water electrolysis*. *ACS Applied Materials & Interfaces, 14*(35), 39820–39828. https://doi.org/10.1021/acsami.2c09004

[31] Zhang, Y., Ouyang, B., Xu, K., Xia, X., Zhang, Z., Ma, J., & Wang, J. (2018). *Prereduction of metal oxides via carbon plasma treatment for efficient and stable electrocatalytic hydrogen evolution*. *Small, 14*(20), 1800340. https://doi.org/10.1002/smll.201800340

Acknowledgement

I am grateful to my supervisor, PhD. Vitali Grozovski, for his time, knowledge, and thoughtful guidance at every stage of this project. Working under his supervision has been a great experience that taught me a lot about both electrochemistry and scientific thinking.

I would also like to thank Dr. Peeter Valk from the Institute of Chemistry for carrying out the SEM and EDS analyses that were central to this work.

Finally, I am deeply thankful to my parents, family, and friends, whose encouragement and support throughout my studies have meant more than I can express.

Annex

Annex 1. Experimental data for apparent Faradaic efficiency calculations

Table A1.1 Experimental data and calculated apparent Faradaic efficiency for NiFe electrodeposition

Sample	Mass before deposition (g)	Mass after deposition (g)	Experimental mass gain, m_{actual} (g)	Faradaic efficiency (%)
NiFe-1	0.18441	0.19599	0.01158	45.86
NiFe-2	0.20273	0.21452	0.01179	46.71
NiFe-3	0.19403	0.20521	0.01118	44.29
NiFe-4	0.21291	0.22458	0.01167	46.22
NiFe-5	0.22020	0.23190	0.01170	46.33
NiFe-6	0.20531	0.21580	0.01049	41.57

The theoretical deposited mass ($m_{theoretical}$) was calculated according to Faraday's law assuming nickel as the primary electroactive species.

Average Faradaic efficiency: 45.16%

Standard deviation: 1.95%

Table A1.2 Experimental data and calculated apparent Faradaic efficiency for NiMo electrodeposition

Sample	Mass before deposition (g)	Mass after deposition (g)	Experimental mass gain, m_{actual} (g)	Apparent Faradaic efficiency (%)
NiMo-1	0.20869	0.21064	0.00195	1.07
NiMo-2	0.18891	0.19143	0.00252	1.38
NiMo-3	0.18701	0.18918	0.00218	1.19
NiMo-4	0.19827	0.20021	0.00193	1.06
NiMo-5	0.21715	0.21936	0.00221	1.21
NiMo-6	0.18040	0.18258	0.00219	1.20

The theoretical deposited mass ($m_{theoretical}$) was calculated according to Faraday's law assuming nickel as the primary electroactive species.

Average apparent Faradaic efficiency: 1.19%

Standard deviation: 0.12%

Annex 2. Tafel slope analysis

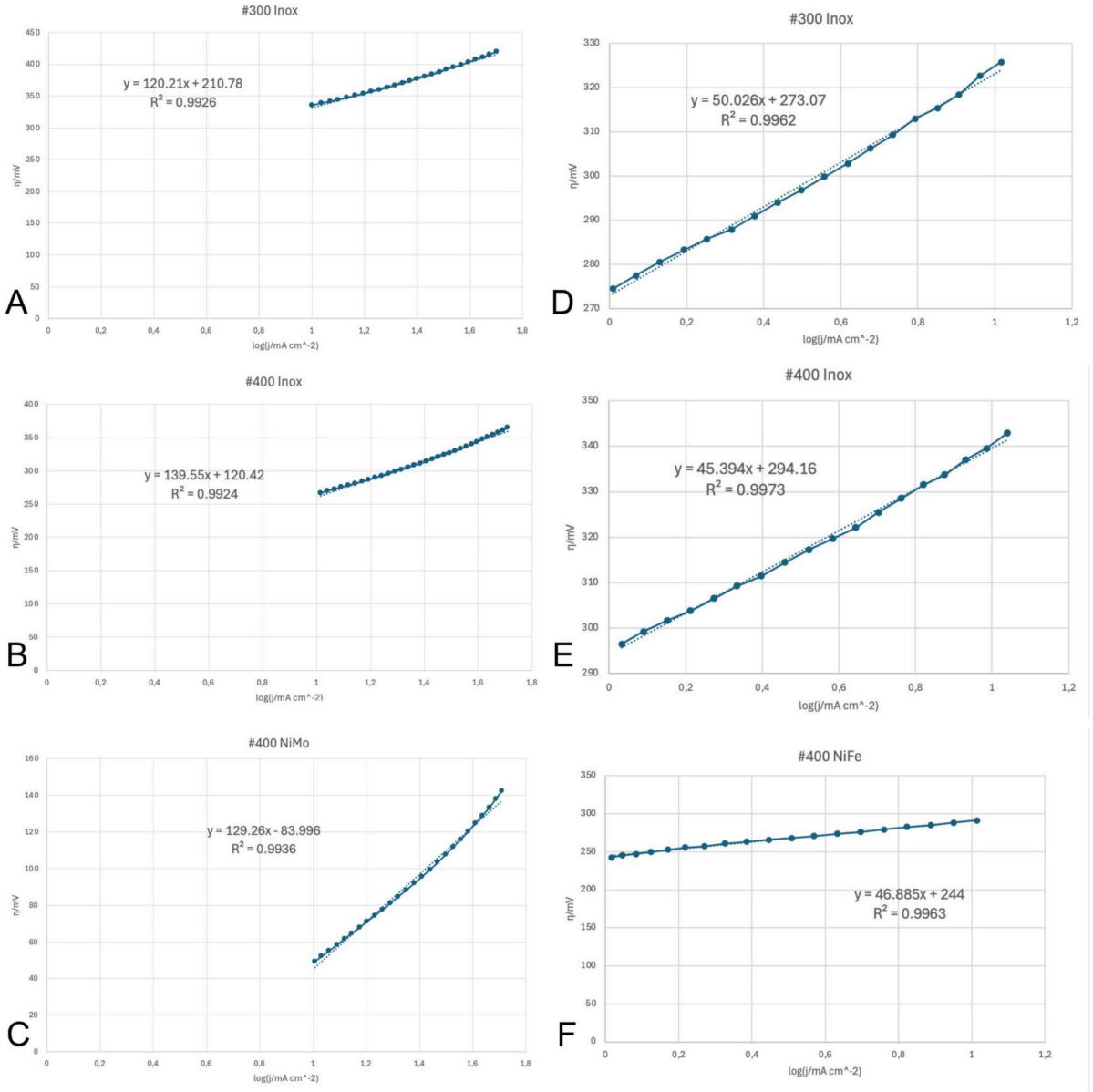

Figure A.2. Tafel plots for HER (A–C) and OER (D–F) measured in 1 M KOH for #300 inox, #400 inox, #400 NiMo, and #400 NiFe electrodes.

OER overpotentials were calculated according to:

$$\eta = E_{RHE} - 1.23\,V$$

Annex 3. Python code sample for automated Tafel slope calculation from HER and OER polarization curves

What This Code Does:

Converts HER and OER potential data into overpotential values

Applies the thermodynamic correction for OER (1.23 V vs. RHE)

Performs linear regression of overpotential versus $\log_{10}$ (current density)

Outputs Tafel slope values and corresponding R^2 coefficients for electrochemical analysis

```
# Required libraries
import numpy as np
from scipy.stats import linregress

# Function for Tafel slope calculation
def calculate_tafel(current_density, potential, reaction="OER"):

# Convert current density to absolute values
current_density = np.abs(current_density)

# Calculate overpotential
if reaction == "OER":

# OER overpotential relative to 1.23 V vs. RHE
overpotential = (potential - 1.23) * 1000

elif reaction == "HER":

# HER overpotential relative to 0 V vs. RHE
overpotential = np.abs(potential) * 1000

else:
raise ValueError("Reaction must be HER or OER")

# Calculate log10(current density)

log_j = np.log10(current_density)

# Linear regression of overpotential vs. log10(current density)
slope, intercept, r_value, _, _ = linregress(log_j,overpotential)

# Return Tafel slope and R² value
return slope, r_value**2
```

Annex 4. SEM–EDS Characterisation

4.1. Bare Stainless Steel Mesh Characterisation

Table A4. EDS elemental composition of bare #300 and #400 stainless steel meshes. Values are reported as mean ± standard deviation from multiple spectra.

Mesh	Ni (wt%)	Fe (wt%)	Cr (wt%)	Mn (wt%)	Si (wt%)	O (wt%)
#300 bare mesh	6.8 ± 1.0	64.9 ± 5.9	16.6 ± 0.8	1.3 ± 0.1	0.4 ± 0.0	0.8 ± 1.1
#400 bare mesh	10.1 ± 1.9	57.4 ± 8.0	15.8 ± 2.0	0.6 ± 0.5	0.4 ± 0.1	1.4 ± 0.6

Carbon was excluded from the summarized composition due to likely contribution from surface contamination and sample preparation. Minor Mo signals detected in the #400 mesh were not included in the final composition because the substrate material was 304 stainless steel.

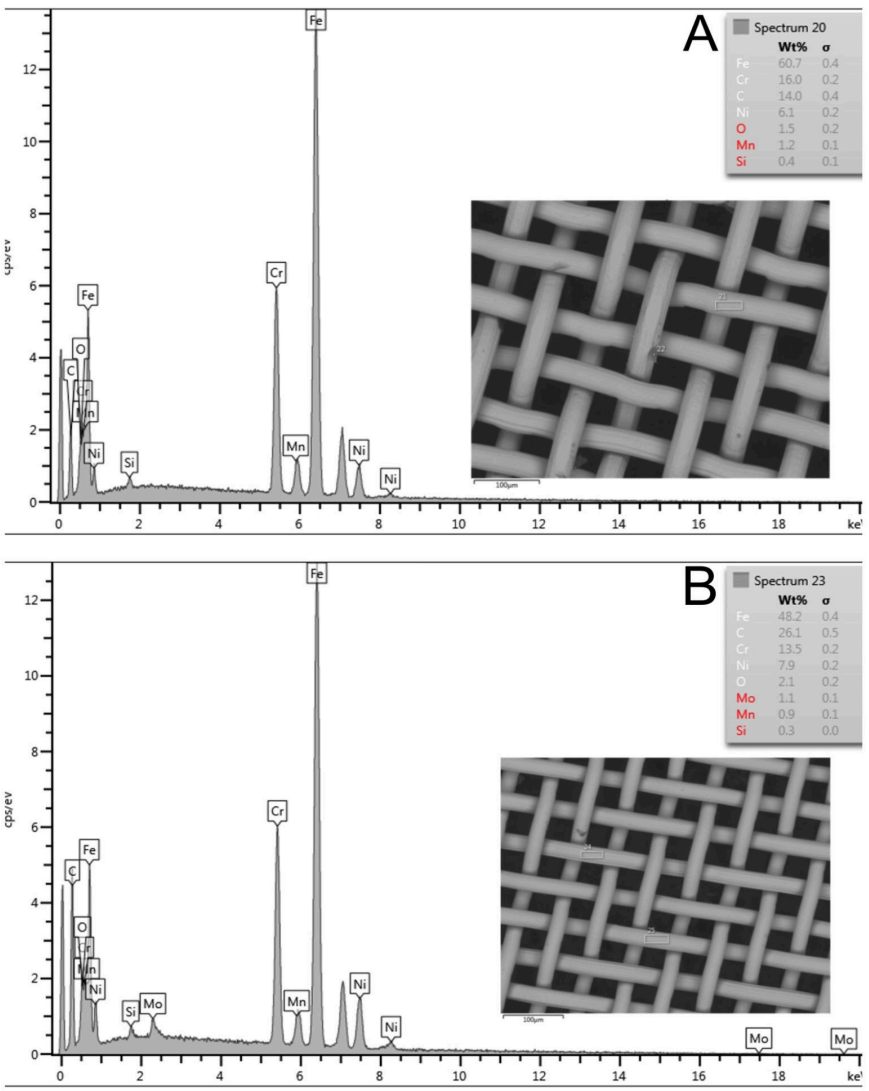

Figure A4.1. Representative SEM micrographs (500×) and corresponding EDS spectra of bare stainless steel meshes: (A) #300 mesh and (B) #400 mesh. Marked regions indicate locations selected for localized EDS analysis. Quantitative elemental compositions reported in Table A4 were obtained by averaging multiple spectra collected from different surface regions.

4.2. SEM–EDS Characterisation of Electrodeposited Coatings before CV

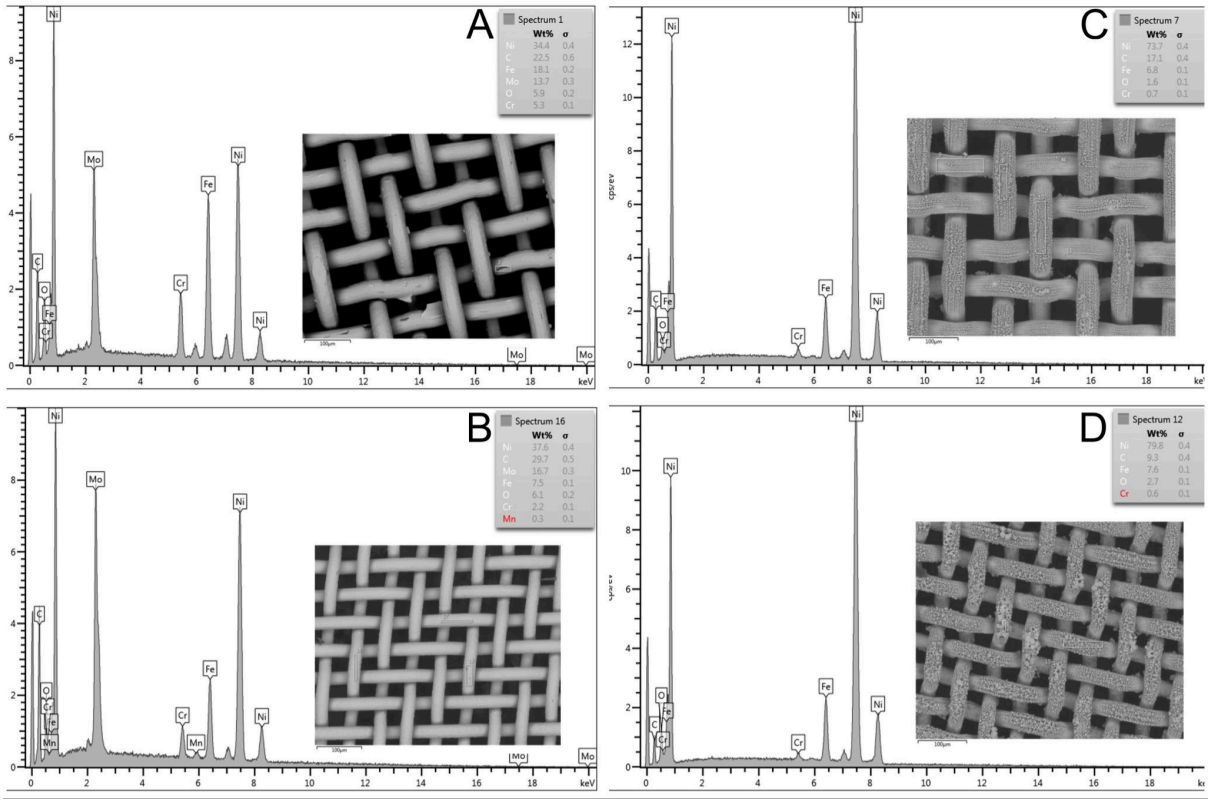

Figure A4.2. Representative SEM micrographs (500×) and corresponding EDS spectra of electrodeposited coatings before cyclic voltammetry: (A) #300 NiMo, (B) #400 NiMo, (C) #300 NiFe, and (D) #400 NiFe. Marked regions in the SEM images indicate locations selected for localized EDS analysis. Quantitative elemental compositions reported in Table 1 were obtained by averaging multiple spectra collected from different surface regions.

4.3. Representative SEM–EDS Spectra of Electrodeposited Coatings after CV

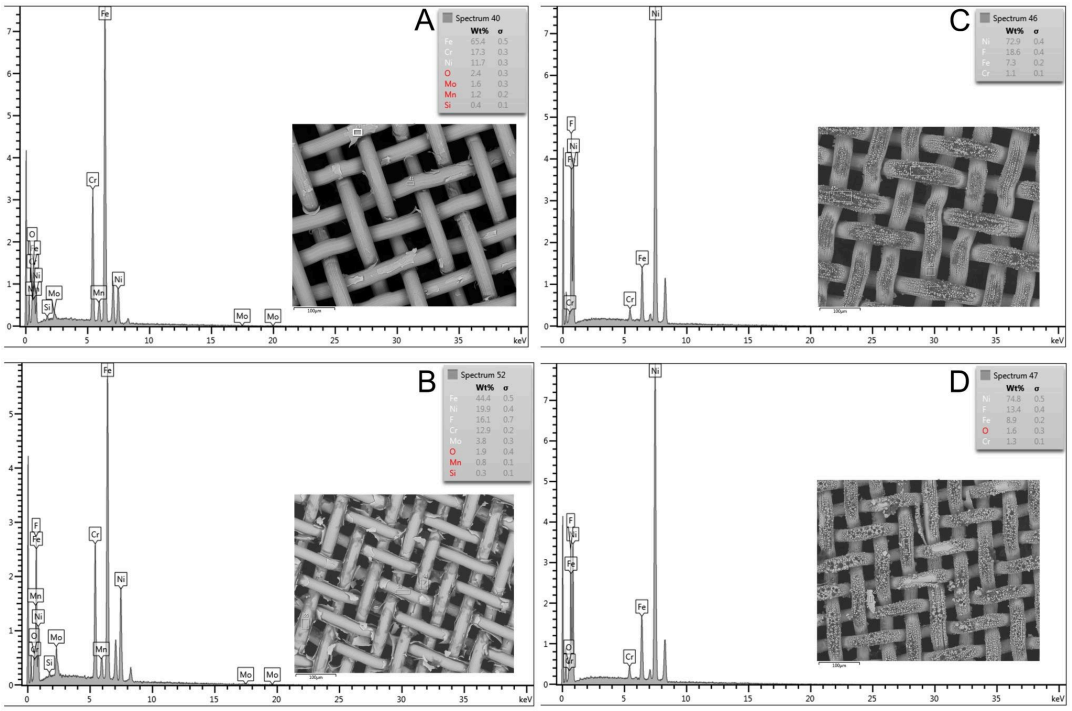

Figure A4.3. Representative SEM micrographs (500×) and corresponding EDS spectra of electrodeposited coatings after cyclic voltammetry: (A) #300 NiMo, (B) #400 NiMo, (C) #300 NiFe, and (D) #400 NiFe. Marked regions in the SEM images indicate locations selected for localized EDS analysis. Quantitative elemental compositions reported in Table 6 were obtained by averaging multiple spectra collected from different surface regions.

4.4 High-Magnification SEM–EDS Maps of Catalyst Coating after Cyclic Voltammetry

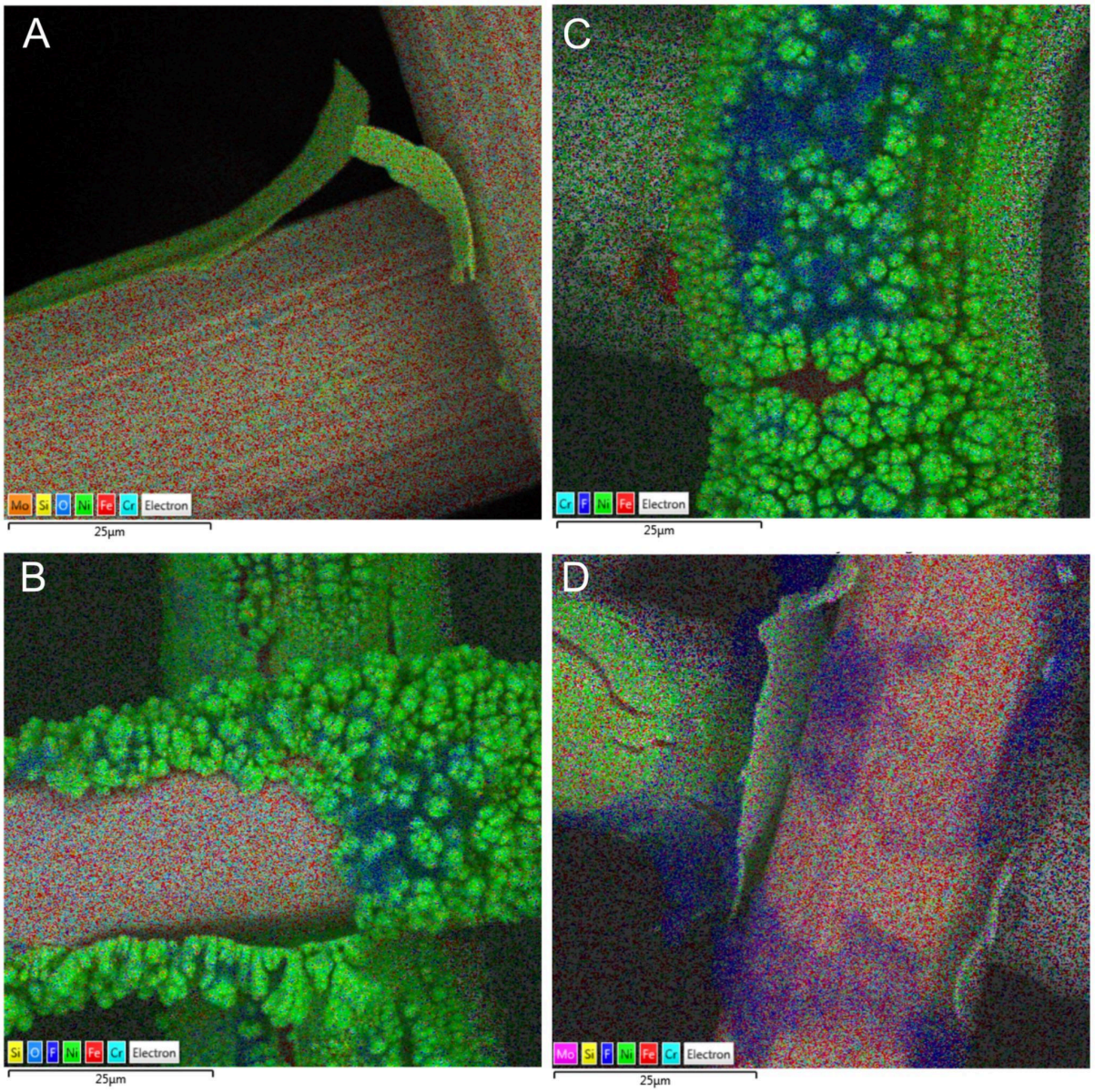

Figure A4.4. High-magnification (3500×) SEM–EDS maps of NiFe and NiMo showing localized degradation and elemental redistribution in electrodeposited coatings after cyclic voltammetry. (A) #300 NiMo, (B) #300 NiFe, (C) #400 NiFe, and (D) #400 NiMo.

NON-EXCLUSIVE LICENCE TO REPRODUCE THESIS AND MAKE PUBLIC

I, Anastasiya Ivashyna,

1. grant the University of Tartu a free permit (non-exclusive licence) to reproduce, for the purpose of preservation, including for adding to the digital archives of the University of Tartu until the expiry of the term of copyright, my thesis

Electrode materials for water splitting in alkaline electrolysis, supervised by PhD Vitali Grozovski;

2. grant the University of Tartu a permit to make the thesis specified in point 1 available to the public via the web environment of the University of Tartu, including via the digital archives, under the Creative Commons licence CC BY NC ND 4.0, which allows, by giving appropriate credit to the author, to reproduce, distribute the work and communicate it to the public, and prohibits the creation of derivative works and any commercial use of the work until the expiry of the term of copyright.

3. I am aware of the fact that the author retains the rights specified in points 1 and 2.

4. I confirm that granting the non-exclusive licence does not infringe other persons' intellectual property rights or rights arising from the personal data protection legislation.

Anastasiya Ivashyna
15/05/2026